https://doi.org/10.5194/egusphere-2025-5110
Preprint. Discussion started: 9 December 2025

Influence of rainfall event characteristics and antecedent conditions on subsurface stormflow response of two forested hillslopes

Emanuel Thoenes[1], Theresa Blume[2], Markus Weiler[3], Bernhard Kohl[4], Luisa Hopp[5], Stefan Achleitner[1]

[1]Department of Infrastructure, University of Innsbruck, Innsbruck, 6020, Austria
[2]Section Hydrology, GFZ Helmholtz Centre for Geosciences, Potsdam, 14473, Germany
[3]Department of Hydrology, University of Freiburg, Freiburg, 79098, Germany
[4]Austrian Research Centre for Forests (BFW), Innsbruck, 6020, Austria
[5]Department of Hydrology, Bayreuth Center of Ecology and Environmental Research (BayCEER), University of Bayreuth, 95440 Bayreuth, Germany

Correspondence to: Emanuel Thoenes (emanuel.thoenes@uibk.ac.at)
Stefan Achleitner (stefan.achleitner@uibk.ac.at)

Abstract. Subsurface stormflow (SSF) is a critical runoff-producing mechanism in many upland and mountainous environments, yet the complex relationships between antecedent conditions, rainfall characteristics and SSF response are still not fully understood. Worldwide, the small number of SSF collection systems (trenches), as well as the generally small number of investigated SSF events limit our ability to generalize the findings and explore the influence of a broader range of storm sizes, intensities, antecedent wetness conditions and different hydrogeologic settings. In this study we present a comprehensive analysis of rainfall and SSF event characteristics as well as antecedent conditions, based on data collected at two forested hillslope sites, where SSF was monitored in research trenches over a 2-year period. Our results show that SSF volume is primarily controlled by total rainfall (P_{tot}) and antecedent wetness, with volumes being up to three orders of magnitude larger under wet initial conditions. At one trench, the volume increased gradually with P_{tot}, whereas at the other trench SSF volume displayed a threshold-like behaviour, likely linked to the irregular topography of the underlying bedrock. The precipitation threshold varied between ca. 15 and 20 mm for wet and dry antecedent conditions, respectively. Peak SSF flow rates of smaller events were influenced by P_{tot} and antecedent conditions, but for larger events ($P_{tot} >$ ca. 20 mm), rainfall intensity was one of the dominant controls along with the rainfall amount preceding peak rainfall intensity. The steepness of the rising limb of the SSF hydrograph was correlated with P_{tot} and rainfall intensity. The antecedent soil moisture index (ASI) together with P_{tot} showed a high correlation with most SSF characteristics. The seasonal analysis revealed that, statistically, the largest SSF volumes occurred in winter, while the highest peak flows and rising rates were observed in spring and summer.

1 Introduction

Subsurface stormflow (SSF) is a key runoff-producing mechanism in many natural landscapes, often contributing significantly to the storm hydrograph of streams (McGuire et al., 2024; Peters et al., 1995; Weiler et al., 2006). Therefore, understanding the controls and processes governing SSF is essential for the future development of more robust rainfall-runoff models, particularly in light of increasingly extreme climatic conditions (Kirchner, 2006; Tabari, 2020; Weiler and McDonnell, 2007). Subsurface flow contributing to storm runoff (i.e. SSF) typically develops when a tilted downslope-oriented layer, horizon or zone with reduced permeability is overlain by a more permeable, unconfined layer or zone so that vertically percolating water is deflected laterally towards the stream (Weiler et al., 2006). Alternatively, SSF can be generated through the "transmissivity feedback mechanism", in which the rise of the water table into a more permeable zone induces a faster, lateral, stream-reaching flow (Bishop et al., 1990; Weiler and McDonnell, 2004). The quick subsurface flow response to rainfall can be coupled to high flow velocities along preferred pathways (preferential flow) as well as to the rapid increase of a more diffuse flow (matrix flow) (Blume and van Meerveld, 2015; Weiler et al., 2006). Preferential SSF occurs when water flows along larger interconnected voids in the matrix (e.g. soil pipes or fractures), through matrix zones characterized by a higher permeability than their surroundings, or in a channelized fashion dictated by the irregular topography of an impeding layer (Anderson et al., 2009; Weiler et al., 2006).

Several factors govern SSF generation, including the characteristics of the macropore and fracture networks, the spatial variation in soil thickness, the topography of surface and impeding layer (i.e. depression storage) and the vertical variation in hydraulic conductivity, which controls the vertical percolation, leakage rate through the impeding layer and the possible onset of faster lateral flow within upper more permeable layers (Hopp and McDonnell, 2009; McGuire et al., 2024). Antecedent wetness conditions further modulate the SSF responses. Wetter soils promote SSF, as they require less additional rainfall to reach saturated or close-to-saturated conditions and initiate lateral flow (Guo et al., 2014; Penna et al., 2011; Uchida et al., 2005). Nevertheless, dry conditions can lead to the formation of soil cracks and support hydrophobicity of soils, both favouring preferential SSF (Buttle and Turcotte, 1999; Peters and Ratcliffe, 1998; Tromp-van Meerveld and McDonnell, 2006a). Rainfall characteristics—including total depth, intensity, and temporal distribution—also play a crucial role. Greater rainfall amounts increase the overall water content and hydraulic head, promoting the connectivity of saturated areas across the hillslope, which enhances SSF generation (Hopp and McDonnell, 2009; Tromp-van Meerveld and McDonnell, 2006b). Hence, the contributing area expands with increasing rainfall amounts, leading to a more uniform hillslope response (Hrnčíř et al., 2010; Šanda and Císlerová, 2009; Tromp-van Meerveld and McDonnell, 2006b).

The relationship between total precipitation amount of an event (P_{tot}) and the resulting SSF volumes (V_{tot}) is often nonlinear, with threshold-like behaviour observed in many studies (Tromp-van Meerveld and McDonnell, 2006a; Uchida et al., 2005; Weiler et al., 2006). SSF can be initiated by a relatively small P_{tot} ("activation" threshold), but significant V_{tot} are typically generated only after P_{tot} exceeds a higher second threshold, which in hillslope studies ranges between ca. 18 and 60 mm (Fu et al., 2013; Tromp-van Meerveld and McDonnell, 2006a; Weiler et al., 2006). Beyond this higher threshold, some studies reported a linear relationship between V_{tot} and P_{tot}, which was most evident for events with wet antecedent conditions, as then differences in soil moisture deficits are minimal (Du et al., 2016; Fu et al., 2013; Noguchi et al., 2001). To account for the influence of the antecedent conditions, some authors studied the relationship with V_{tot} considering a combined variable, comprising rainfall volume and antecedent soil moisture index (ASI), which facilitated the threshold detection and increased the observed correlation (Fu et al., 2013; Han et al., 2020). Similar results were also observed at the catchment scale for the total stormflow volume (Detty and McGuire, 2010; Wei et al., 2020; Zwartendijk et al., 2023).

At the hillslope scale, precipitation intensity is generally not correlated to V_{tot} (Fu et al., 2013; Tromp-van Meerveld and McDonnell, 2006a). Nevertheless, rainfall intensity—especially peak intensity—is often, but not always (e.g. Tromp-van Meerveld and McDonnell, 2006) correlated with peak flow. Noguchi et al. (2001) observed how for macropore flow this relationship was strong for some macropores but weak for others, whereas it was good for the matrix flow. In both cases, the correlation decreased for events characterized by drier initial conditions. Fu et al. (2013) describe how, if events with small intensities and large ASI were excluded, a threshold between the max. 30-min intensity and peak flow was present. Moreover, Uchida et al. (2005) found that once pipe flow occurred, its maximum flow rate was sensitive to the maximum rainfall intensity. All these studies highlight the complex relationship between initial conditions, rainfall intensity, P_{tot} and peak flow of SSF. The lag time between rainfall (centroid or peak intensity) and peak flow depends on multiple factors, including peak rainfall intensity, cumulative rainfall preceding the peak, antecedent conditions, as well as the runoff producing mechanism. Haga et al. (2005) observed that once the upslope saturated area was large, the lag time decreased with increasing rainfall intensity, indicating that the lag time is also affected by the timing of the peak rainfall (i.e. the state of the system preceding the higher intensities). The size of the contributing area also affects the stormflow response, as smaller areas were associated with a quicker response (Haga et al., 2005). On the other hand, the area drained by the SSF-collecting trench was shown to be influenced by rainfall intensity, rainfall amount and initial conditions (Hrnčíř et al., 2010). A quick response can also be generated through fast macropore flow, which depending on the networks characteristics and its connection to the surface can be more or less influenced by the initial conditions and rainfall intensities (Buttle and Turcotte, 1999; Uchida et al., 2005;

Weiler and Naef, 2003). Zhang et al. (2021) observed a negative power function between peak intensity and lag time, with variability in lag times increasing when rainfall intensities were below a critical threshold. All the presented studies highlight the complex relationships between the SSF response, rainfall characteristics and antecedent conditions.

Despite our improved understanding of the controls of SSF, the limited number of study sites hinders our ability to further explore SSF and generalize the findings. At the hillslope scale, SSF has been investigated using non-invasive geophysical methods such as electrical resistivity tomography (Hübner et al., 2017; Uhlemann et al., 2024) and ground-penetrating radar (Guo et al., 2014), hydrometric measurements (wells, piezometers, tensiometers, soil-moisture sensors) (Du et al., 2016; Heller and Kleber, 2016), dye staining and excavation (Anderson et al., 2009), and, in particular, trenches excavated perpendicular to the slope (Buttle and Turcotte, 1999; Fu et al., 2013; McGlynn et al., 2002; Netto et al., 1999; Tromp-van Meerveld and McDonnell, 2006a; Uchida et al., 2005). Dyes, salts and stable water isotopes are commonly used as tracers to gain insights into flow-network characteristics, travel-time distributions and the interactions between matrix and preferential flow (Angermann et al., 2017; Kienzler and Naef, 2008; Tsuboyama et al., 1994).

Numerical modelling, when combined with experimental findings and conceptualizations, whether used to simulate real events (Meerveld and Weiler, 2008; Wienhöfer and Zehe, 2014) or to conduct virtual experiments (Hopp and McDonnell, 2009; Weiler and McDonnell, 2004), provides a complementary way to explore how surface and subsurface properties, antecedent conditions, and rainfall characteristics control the SSF response. Despite the many approaches available to explore SSF, trenched hillslopes remain a cornerstone of SSF research, as they are the only way to measure SSF directly and as a continuous time series of flow. However, due to the high installation costs and time-consuming maintenance, only a handful of research trenches have been excavated worldwide (Blume et al., 2025; Blume and van Meerveld, 2015). Moreover, the small number of SSF events analysed in most studies further limits the ability to explore the influence of a broader range of storm sizes, intensities and antecedent conditions. Especially the number of large, threshold-exceeding events is usually small. Additionally, many existing studies focus primarily on total SSF volume and its relationship with P_{tot}, rainfall intensity and antecedent conditions, while peakflow is not always considered and other metrics as rising rate and response/lag time are often neglected in the analysis. As a consequence, to the best of the authors' knowledge, a comprehensive correlation analysis between all these metrics has not been carried out so far. Thus, this work aims to expand the knowledge of how rainfall event characteristics, antecedent conditions and SSF event characteristics (including peakflow, rising rate and response/lag time) are correlated, by analysing two years' worth of data collected at two trenches with contrasting hydrogeological settings (shallow and deep bedrock). The main research questions tackled in this study are: (1) What is the influence of rainfall depth and intensity on the subsurface stormflow response? (2) To what degree do the initial conditions (initial soil moisture and initial trenchflow) control the SSF response? (3) What is the relationship between different SSF event characteristics? (4) Does the SSF response vary seasonally?

2 Methods

2.1 Site Description

Three trenches to capture SSF were installed in a headwater catchment in the Black Forest, southwest Germany (47°57' N, 7°50' E). For this analysis, we focussed on the two trenches with the most comprehensive data set: trench 1 and trench 3 (T1 and T3). The two trenches were excavated on two hillslopes located in a zero- and a first order sub-catchment of the research catchment. T1 and T3 are each situated near small perennial streams (Figure 1); the trench elevations are ca. 370 and ca. 400 m asl, respectively. The hillslope of T1 is predominantly planar, while the one at T3 is concave. The average slope of the instrumented area, which extends up to ca. 25 m above the trench, is 19° for T1 and 27° for T3.

https://doi.org/10.5194/egusphere-2025-5110
Preprint. Discussion started: 9 December 2025

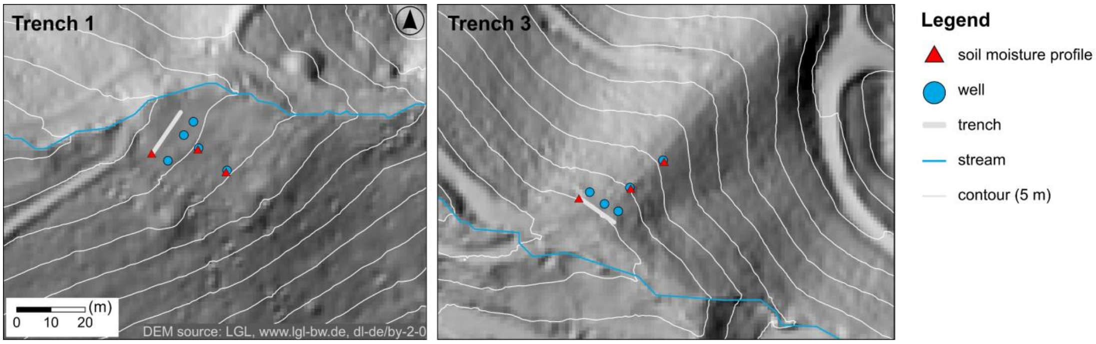

Figure 1. Location of the trenches, wells, soil moisture profiles and streams.

The climate is temperate, without a dry season and characterized by warm summers according to the Köppen classification (Cfb) (Peel et al., 2007). The mean annual temperature and precipitation is 11°C and 836 mm, respectively (2003–2023; weather station of the German Meteorological Service (DWD) in Freiburg located ca. 7 km north from the study area). The summer months May to August are characterized by the highest mean monthly rainfall as well as the highest mean rainfall intensity (convective storms) (2003–2023; DWD Freiburg).

The bedrock is formed by Migmatite and Paragneiss at T1 and by Migmatite at T3 (LGRB-Kartenviewer, 2024). In both locations the bedrock is overlain by unconsolidated periglacial slope deposits (colluvium) in which Cambisols have developed. T1 was excavated into the colluvium and does not reach the bedrock. From the surface down to 0.6 m below ground level (BGL) (depth of deepest soil sample), the soil is characterized by a high concentration of angular granule to cobble-sized clasts (i.e. diameter > 2–256 mm) supported by a loam matrix (see Table 1 for soil properties). From 0.6 m BGL to the base of the trench the visual inspection showed an overall homogeneous material. Of particular interest is the soil colour of the trench face, which is not homogeneous. Besides the expected darker brown upper layer, a vertical ca. 2–3 m wide zone located on the southwest (right) side of the trench is characterized by a distinct dark bluish-grey colour. This coloration, which continues northeast (left) along the bottom portion of the trench, is a clear indication of waterlogged soils (Smirnova and Kozlov, 2023). The colour is typical of iron compounds that form in saturated soils under anaerobic (reducing) conditions (Schmidt and Ahn, 2019). The presence of such a long-lasting saturated zone matches well with our trenchflow and water level observations. The saturated zone extends up to ca. 4.5 m upslope from the trench to the location of a small intermittent spring.

At T3 the top 0.4 to 0.6 m of the colluvium is very poorly sorted and mainly composed of large (up to cobble-sized) angular clasts with a sandy loam matrix (see Table 1). Below this zone the amount and size of larger clasts gradually decreases (inverse grading) and the soil becomes more homogeneous and richer in silt (loam). This textural change is also supported by the water-retention analysis and soil density measurements of soil sampled at the trench face. The base of the colluvium is defined by the weathered bedrock. At the trench the interface between colluvium and bedrock dips towards northwest (left trench side) while the elevation of the ground surface remains somewhat constant. This translates to an increase in thickness of the colluvium from a few decimetres on the right side of the trench to more than 2 m on the left side of it. The thickness of the coarser upper layer remains fairly constant throughout the trench. Drilling samples of boreholes located ca. 12 and 21 m upslope of the trench also showed the presence of this coarse upper layer (thickness ca. 0.25–0.6 m) overlying a finer, more homogeneous sediment. This suggests that the hillslope directly above the trench is covered by a mostly continuous coarse-grained and thus highly permeable layer overlying a finer, less permeable one. The bedrock´s permeability is classified as very low according to thematic geological maps (LGRB-Kartenviewer, 2024) and thus likely acts as an aquitard/aquiclude in this hydrogeological setting.

The two hillslopes are covered by a mixed forest. The canopy above T1 is dominated by hornbeam (*Carpinus*) and spruce (*Picea*), interspersed with a few ash (*Fraxinus*) and beech (*Fagus*) trees. With higher elevation the proportion of coniferous trees increases giving rise to a coniferous-dominated forest. Young spruce trees make up most of the understory which is moderate above the trench and thins out further upslope. Strong winds toppled a few trees (mostly hornbeam) on the outer northern part of the hillslope during the observation period.

At T3 a mix of predominantly hornbeam (*Carpinus*) and fir (*Abies*) is found with a few robinia (*Robinia pseudoacacia*) and ash (*Fraxinus*) on the lower part of the hillslope. The understory is thin and made up mainly of young fir trees. On both hillslopes the forest floor is covered by litter of deciduous and needle leaves as well as by some deadwood.

Table 1. Soil Properties at trench 1 and 3

depth (m BGL)	gravel (%)		sand / silt / clay (%)		bulk density (g cm^{-3})		loss on ignition (%)		porosity (-)	
	T1	T3	T1	T3	T1	T3	T1	T3	T1	T3
0.1	65	56	43.3 / 31.7 / 25.0	57.5 / 25.7 / 16.8	1.1	1.2	7.4	6.0	0.57	0.54
0.3	63	65	41.6 / 34.2 / 24.2	66.2 / 20.6 / 13.2	1.3	1.3	4.2	6.0	0.52	0.51
0.6	77	55	51.7 / 33.7 / 14.6	54.6 / 26.5 / 19.1	1.7	1.2	2.2	3.8	0.34	0.52
1.5		77		44.6 / 41.9 / 13.5		1.9		1.7		0.29
2.0		77		52.4 / 34.6 / 13.0		1.9		2.1		0.25

analysis method: skeleton = dry sieve, sand = wet sieve, silt and clay = laser diffraction, porosity = from fitted water retention curve obtained from HYPROP 2 and WP4C (METER-Group) measurements

2.2 Experimental Design

Two slope-perpendicular trenches, measuring 11 and 14 m in length and up to 2–3 m in depth, were installed to quantify SSF (Table 2). As illustrated in Figure 2, SSF was collected from two different depth horizons using drainage mats positioned along the trench face. At the bottom of the drainage mat a pond liner was inserted 5–10 cm into the trench face with an upward angle. The pond liner was then folded around a drainage pipe, forcing the collected water into the pipe (see cross section in Figure 2). The pipes were slightly tilted to route the water to the measuring equipment. Once the drainage system was installed, the trench was backfilled. The geometry of the two trenches (see Table 2) differs due to the different site characteristics.

The trench discharge (trenchflow) was gauged using a set of two custom-built tipping buckets. Each tipping bucket is able to measure flowrates of up to ca. 450–500 l/h, although the accuracy notably decreases beyond a discharge of ca. 300 l/h. Since discharges greater than 450 l/h were sporadically observed at the bottom section of T3, a custom-made V-Weir, built following the design proposed by Stewart et al. (2015), along with a vented pressure transducer (Truebner GmbH), was installed towards the end of the study period (27 Mai 2024–25 June 2024). Along with the flow rate, the temperature and electrical conductivity of the trenchflow was also continuously measured. Above the trench, the shallow groundwater level was monitored using five observation wells; three wells were aligned 2–5 m above the trench and an additional two were located ca. 10 m and 20 m further upslope. The 6 cm-wide well boreholes were drilled using a hand-held percussion hammer. The depths of the boreholes vary between 1 to 4 m, as difficult drilling conditions (e.g. large boulders) sometimes limited the drilling depth (tool refusal depth). All boreholes were equipped with 5 cm diameter, fully slotted PVC pipes wrapped in geotextile. Where possible, the annular space between pipe and borehole wall was filled with quartz sand (≤ 2 mm). Each well was equipped with a capacitance water level sensor or a pressure transducer (Truebner GmbH) to monitor the water level. The water content and temperature of the soil was measured in three vertical profiles with TDT sensors (SMT100, Truebner GmbH). The deepest profile (2–2.5 m) was installed along the edge of the trench-face a few decimetres away from the drainage mat (Table 2). The two shallower profiles were set up near the two upper wells and had sensors installed at 10, 30 and 60 cm BGL. All trench data (trenchflow, electrical conductivity, temperature, water level and water content) were continuously measured, predominantly using a 10-minutes logging interval.

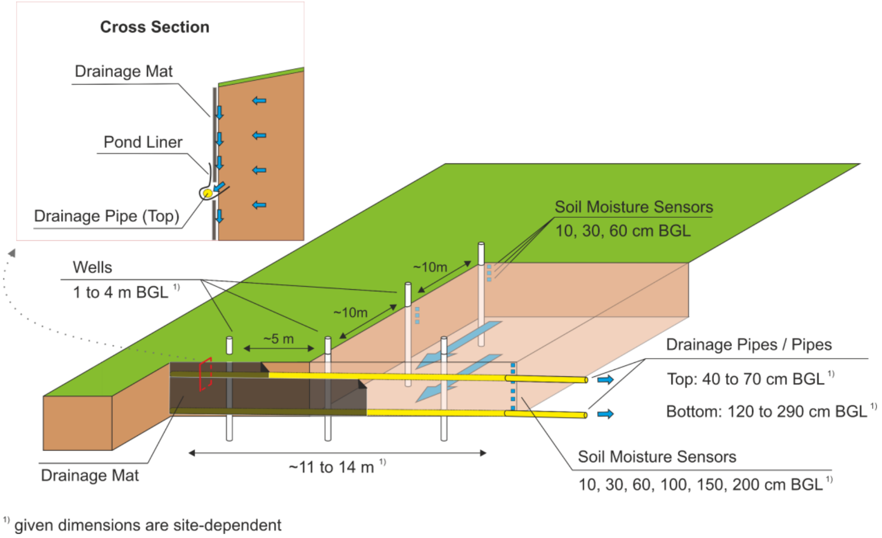

Figure 2. Experimental design of the trenches. Blue arrows show water flow directions.

Table 2. Trench properties

Properties	T1	T3
Trench total depth (m)	2.7 – 2.9	1.2 – 2.1
Upper section depth (m)	0.5 – 0.7	0.4 – 0.6
Trench width (m)	14.4	11.0
Soil moisture sensors depth (m)	0.1 / 0.3 / 0.6 / 1.5 / 2.0 / 2.5	0.1 / 0.3 / 0.6 / 1.0 / 1.4 / 2.0

Meteorological data was collected from a weather station set up in an open field near T1 and ca. 500 m from T3 at an elevation of ca. 350 m asl (47°57'25" N; 7°50'17" E). Rainfall was measured with a tipping bucket rain gauge (Thies) using a 5 min interval. Two gaps in the timeseries (12% of the total rainfall data) were filled with data from a station located ca. 2 km N-NW, equipped with a tipping bucket rain gauge (Young 52203). An event-based comparison between the two stations showed good agreement in the precipitation data, despite the secondary station being operated with a 10 min logging interval.

2.3 Data analysis

2.3.1 Data pre-processing

The analysed data was collected over a period of ca. 2 years from 25 August 2022 to 1 October 2024. The trenchflow data used for the analysis required some pre-processing. Short data gaps in the timeseries of T1 and T3 (e.g. due to sensor maintenance) were filled using linear interpolation. Besides a few exceptions, most gaps were shorter than 2 h. Outliers were filtered out and the gaps filled using the same linear approach. Longer gaps (e.g. due to sensor failure) were not filled and excluded from the analysis. Nearly all the data was recorded using a 10 min interval with some exceptions of 15 and 20 minutes. Therefore, to homogenize the timeseries the time was resampled into 10 min intervals using a linear interpolation approach. Since this study focuses on liquid precipitation, periods characterized by snowfall and snowmelt were excluded from the analysis (10 December 2022–19 February 2023 and 5 January 2024–22 January 2024). These periods were identified based on data from a nearby snow-measuring DWD weather station (Freiburg) as well as field observations and trenchflow data. Only periods with data available for both trench sections (top and bottom) were considered. During a handful of events trenchflow exceeded the capacity of the tipping buckets of ca. 450–500 l/h leading to erroneous plateaus in trenchflow. These events were not included in the analysis. Nonetheless, a few exceptions were made for events that were not obviously cut off despite the observed extremely high flow rates.

The rainfall timeseries, derived from the two weather stations (see previous section), was resampled using a 5-minute interval. Soil moisture dynamics were monitored using SMT100 sensors (Truebner GmbH), which measure temperature and dielectric permittivity. The volumetric water content (VWC) was derived using the Complex Refraction Index Model (CRIM) to account for the influence of temperature on permittivity (see Appendix A for details). Short data gaps in the resulting VWC timeseries (e.g. due to sensor maintenance) were filled using a linear interpolation approach, while longer gaps were not filled. Most gaps were shorter than 2 hours.

2.3.2 Rainfall Event Delineation

To carry out the event-based analysis, events had to be delineated from the continuous rainfall timeseries. For this purpose, the commonly used minimum inter-event time (MIT) method in conjunction with the minimum rainfall depth (MRD) criteria was applied (Dunkerley, 2008). According to the MIT method, each rainfall event has to be preceded and succeeded by a fixed minimum dry period (MIT) (Brasil et al., 2022). In other words, two rainfall occurrences are considered part of the same event if they are separated by a time period shorter than the MIT. In the literature MIT values range from 3 min to 24 h depending on the site and application, and although values between 6 and 8 h are the most commonly adopted it is evident that no recommended MIT value exists (Dunkerley, 2008). Despite this, the MIT value heavily influences the number of delineated rainfall events as well as their characteristics (e.g. duration, depth, intensity) (Brasil et al., 2022). Therefore, different MITs were applied to our dataset and the results were evaluated. In our case, an MIT of 6 h yielded the most satisfactory results, as each SSF initiation was mostly associated with a single well-defined rainfall event and a relatively low number of single-tip events (i.e. events consisting of only one bucket tip) was generated. In comparison, longer MITs generated larger rainfall events spanning multiple SSF initiations while shorter MITs led to a greater segmentation of sometimes clearly associated rainfall pulses. Once the events were delineated (MIT of 6 h), the MRD criteria was applied to eliminate single-tip events, resulting in an MRD of 0.105 mm in our case.

2.3.3 Subsurface Stormflow Event Delineation

Several methods from manual to fully automatic have been developed to delineate storm events from continuous streamflow records (Millar et al., 2022). However, most automatic and semi-automatic methods were developed for larger rivers, not for small, flashy, intermittent headwater creeks, whose complex flow dynamics more closely resemble those observed at the trenches (trenchflow). As a result, these methods often require somewhat smoother hydrographs, the presence of a continuous baseflow and in some cases well-defined recession limbs (Blume et al., 2007; Koskelo et al., 2012; Mei and Anagnostou, 2015). Additionally, only a handful of these methods integrate precipitation data linking rainfall events to stormflow events (Koskelo et al., 2012; Mei and Anagnostou, 2015). Automated methods for delineating SSF events based on trenchflow signal (e.g. not using a nearby stream to define the start and end of stormflow events) were not found in literature; authors dealing with trenchflow hydrographs generally use manual delineation methods or at least do not mention the use of automated methods (e.g. Fu et al., 2013; Han et al., 2020; Tani, 1997).

In this study, due to the long time series and to ensure the most objective delineation possible, a semi-automatic separation method was developed. The new method was tailored to the observed trenchflow, which was flashy, quite noisy and characterized by periods with and without “baseflow”. Furthermore, the method allowed to link rainfall events to SSF events and further classify them. It scans the trenchflow time series from the start of each rainfall event, and if the onset of an SSF event is detected, it links the two. If baseflow is absent, the onset of flow marks the event start. If baseflow is present, the start is detected by assessing the increase in discharge over two time windows (short and long) relative to a threshold. The end of

https://doi.org/10.5194/egusphere-2025-5110
Preprint. Discussion started: 9 December 2025

SSF events is detected by analysing the change in discharge and its standard deviation over a fixed time window as well as considering the flowrate preceding the events. The delineation method is described more in detail in Appendix B.

The automatic delineation results were satisfactory. For T1 and T3 on average only ca. 4% of the starts had to be added, 15% had to be removed and 12 % had to be re-positioned, while 21% of the ends had to be re-positioned.

2.3.4 Classification of Subsurface Stormflow Events

After the detection of starting and ending points in the trenchflow time series, the events were classified into simple events and subevents (Figure 3). Simple events are "stand alone" events that do not overlap with the preceding or subsequent events and are triggered by one rainfall event. Subevents are also associated with a triggering rainfall event but, unlike simple events, overlap with events detected before and/or after (i.e. they might start before the end of the preceding event and/or end after the start of the subsequent event) and thus are part of a larger, more complex event. For this reason, two or more overlapping events (i.e. subevents) are grouped into so-called complex events.

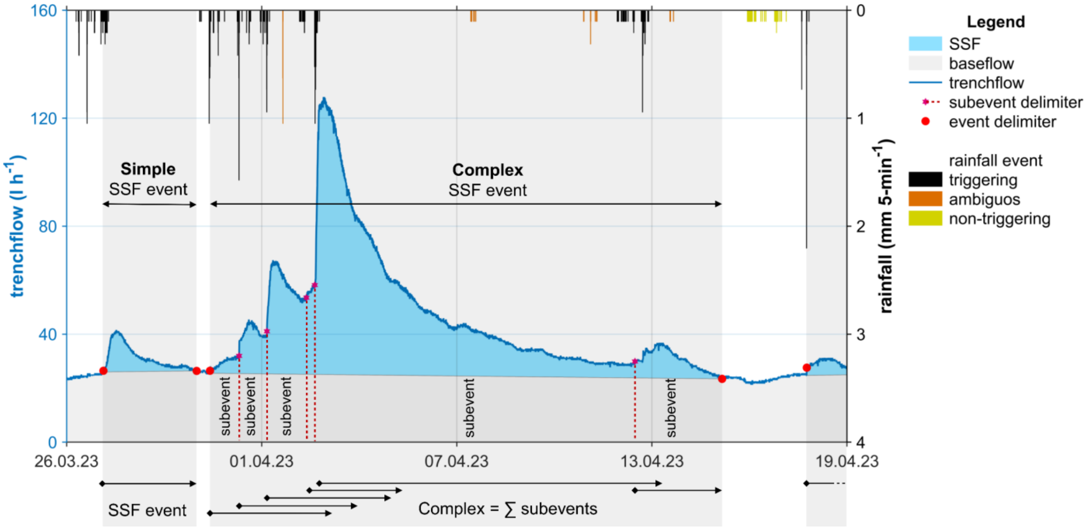

Figure 3. Classification of SSF and rainfall events

2.3.5 Rainfall Event Classification

Rainfall events are classified into three categories: triggering, ambiguous and non-triggering (Figure 3). Triggering events are all rainfall events that trigger SSF events (simple events and subevents), and are therefore linked to the start of SSF events. Ambiguous events are events that occur within SSF events but for which no SSF starting point could be detected (i.e. they do not lead to a noticeable increase in trenchflow); nevertheless, they may contribute to the event-trenchflow. Finally, non-triggering events are events that neither induce nor contribute to SSF events and therefore occur outside of delineated SSF events.

2.3.6 Event Characteristics

For each rainfall event the total depth (P_{tot}), mean intensity (I_m), I_5, I_{30} and I_{60} (i.e. max. 5-, 30- and 60-min rates) were calculated. For rainfall events that occurred during the period covered by the secondary weather station, I_5 was not considered due to the 10-minute logging interval of this station. For simple and complex SSF events, the associated total rainfall (P_{tot}) was calculated by summing the depths of all triggering and, where present, ambiguous events linked to the SSF event. The rainfall intensities (I_m, I_5, I_{30} and I_{60}) of the triggering events associated with the same complex SSF event were additionally averaged. This averaging was performed to examine how rainfall intensity influences properties (e.g. total volume) related to the entire complex event. The mean trenchflow ($\bar{Q}$), total SSF volume (V_{tot}) and minimum contributing area (MCA) were calculated for simple and complex SSF events. The total SSF volume was computed without considering the baseflow, which was separated from the event runoff using the straight line method (Figure 4) (Maidment, 1995). Following this method, the timestep preceding the start of the event and the endpoint were connected through a straight line. The minimum contributing area (MCA), also called stormflow ratio, was calculated, as described by Dickinson and Whiteley (1970), as following:

$$\text{MCA} = V_{tot} \;/\; P_{tot} \qquad (1)$$

The remaining metrics ($Q_{\Delta max}$, time to peak, rising rate, response time and lag time) were calculated for simple events and subevents (Figure 4). The maximum increase in trenchflow ($Q_{\Delta max}$) is the difference between the max. observed trenchflow and the initial trenchflow (Q_i) (i.e. flow preceding the event; see also Section 2.3.7 Antecedent Conditions). The time to peak is defined as the period between the timestep preceding the start of the event and the max. trenchflow (peak flow), while the rising rate is calculated as $Q_{\Delta max}$ divided by the time to peak. Very small events having $Q_{\Delta max} < 3$ l/h were not considered for the rising rate calculations. The response time refers to the interval between the centroid of the rainfall event and the start of the SSF event, whereas the lag time is the time between the centroid and the maximum observed trenchflow.

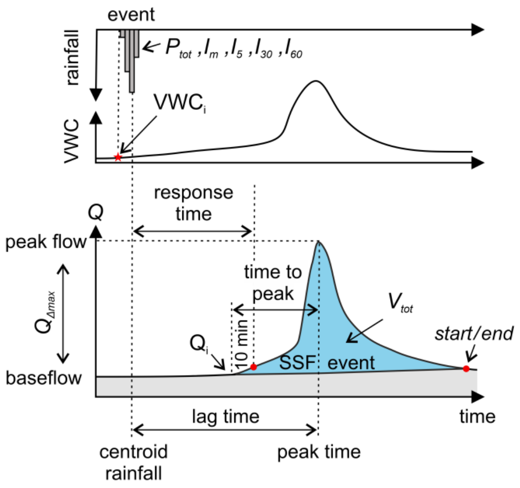

Figure 4. Definition sketch for the event-based analysis

In five cases, the rising phase of a subevent was interrupted by a successive subevent, preventing the potential peakflow of the preceding subevent from being reached. As a result, for these subevents the peak-dependent metrics were not considered. Moreover, occasionally simple events and subevents were characterized by a well-defined double peak with a higher second peak. In these and other exceptional cases (10 events) the $Q_{\Delta max}$ was used in the analysis but the time-dependent metrics (e.g. rising rate) were not, as the double peak nature of the event would lead to inconsistent results.

2.3.7 Antecedent Conditions

The antecedent wetness of the subsurface preceding the SSF events was characterized using soil moisture and trenchflow data. More specifically, the initial average volumetric water content (VWC_i), antecedent soil moisture index (ASI) and initial trenchflow were considered.

The VWC_i was calculated using a weighted average approach as described in Pangle et al. (2014):

$$\text{VWC}_i = \frac{\sum_{j=1}^{6} \theta_j H_j}{H_{\text{tot}}} \qquad (2)$$

where θ_1 to θ_6 represent the volumetric water content measured at different depths (see Table 2), H_1 to H_6 are the soil volumes (heights) that each sensor is assumed to represent, and H_{tot} is the total considered depth. For each sensor, H is calculated by dividing the distance between the sensor above and below by two. For the uppermost and lowermost sensors, the distance from the adjacent sensor was used. For example, for sensors depths of 10, 30, 60, 150, 200 and 250 cm the associated H would be 20, 25, 60, 70, 50 and 50 cm, respectively, and the total depth 275 cm. Since the soil moisture at 10, 30 and 60 cm BGL was measured at three different locations (i.e. at three soil moisture profiles: B1, B2 and B3), a mean value for each depth was computed and used in the depth-averaging procedure described above. Periods with missing or unreliable data were handled differently depending on the depth of the affected sensor. If sensors installed at depth 4, 5 or 6 had a data gap the $\mathrm{VWC_i}$ was not computed for that time period. On the other hand, for the shallower depths 1, 2 and 3 (i.e. 10, 30 and 60 cm BGL) if data from one or two sensors was missing, data from the remaining working sensor/s was used. The Antecedent Soil-moisture Index (ASI) was calculated using the following equation (Haga et al., 2005; Penna et al., 2015):

$$\mathrm{ASI} = \bar{\theta}_s \times D \tag{3}$$

where $\bar{\theta}_s$ is the shallow average VWC ($\mathrm{m^3/m^3}$) calculated for the three upper soil moisture sensors (depth 1, 2 and 3) using Eq. 2 and D is the total considered depth in mm (i.e. 750 mm). The ASI, which represents the water stored in the upper soil layer, can be added to the total precipitation depth (P_{tot} + ASI), allowing us to describe the total rainfall and initial soil moisture conditions using one value. Nevertheless, if the ASI is too large, the effect of the initial conditions can be over-represented in the composite variable P_{tot} + ASI. We therefore introduced a second composite variable where ASI is weighted: P_{tot}+$\mathrm{ASI_{adj}}$ (see section 2.3.8). Both the $\mathrm{VWC_i}$ and ASI were computed for the timestep preceding the triggering rainfall event. The trenchflow before the start of SSF events was also considered. The initial trenchflow (Q_i) was computed by averaging the flow over a period of 30 minutes preceding the start of the SSF event. For complex SSF events the initial trenchflow of the first subevent was considered.

2.3.8 Correlation Analysis

The Spearman rank correlation coefficient was used to quantify the degree of correlation between the metrics describing rainfall event characteristics, antecedent conditions, and SSF event characteristics. The correlation with the composite variable (P_{tot} + ASI) was also computed. However, since the results suggested that ASI was overrepresented in the composite variable, ASI was adjusted ($\mathrm{ASI_{adj}}$) using a metric-specific weighting factor (w), which was optimized to maximize the Spearman correlation of the composite variable (P_{tot} + w·ASI) with the other SSF metrics. The Spearman rank correlation was used for the analysis in order to capture any monotonic relationship, as the observed relationships were sometimes nonlinear (e.g. exponential) and thus would have not been identified by the more restrictive Pearson correlation analysis. The correlations were considered not significant when the p-value was larger than 0.05.

Furthermore, to explore how the observed increase in MCA with P_{tot} translates into the relationship between V_{tot} and P_{tot}, we first performed a linear regression of MCA against P_{tot} (Eq. 4):

$$MCA = \frac{V_{tot}}{P_{tot}} = a \cdot P_{tot} + b \tag{4}$$

Since MCA is defined as the ratio of V_{tot} to P_{tot}, this regression implies a corresponding V_{tot}–P_{tot} relationship obtained by multiplying Eq. 4 by P_{tot} (Eq. 5). This formulation is consistent with the hydrological relationship V = area · P, where the (effective) contributing area is represented by MCA.

$$V_{\mathrm{tot}} = \mathrm{MCA} \cdot P_{\mathrm{tot}} = a \cdot P_{\mathrm{tot}}^2 + b \cdot P_{\mathrm{tot}} \tag{5}$$

We then plotted the V_{tot}–P_{tot} curve given by Eq. 5 (using the coefficients a and b derived from the fitted Eq. 4) together with the observed V_{tot}–P_{tot} data, and compared it to the fit of a simple linear regression of V_{tot} on P_{tot}. This approach allowed us to

https://doi.org/10.5194/egusphere-2025-5110
Preprint. Discussion started: 9 December 2025

illustrate how the observed increase in MCA with P_{tot} manifests in the V_{tot}–P_{tot} relationship. This analysis was performed separately for events with dry and wet antecedent soil moisture conditions. To classify the events, the observed range of VWC_i was divided into four equal intervals. Events with VWC_i values within the upper quarter of this range were classified as wet, while those below the upper quarter were classified as dry. The statistical analyses were carried out using MATLAB (The MathWorks Inc, 2021).

3 Results

3.1 Rainfall events characteristics

During the observation period a total of 236 and 262 rainfall events were analysed for T1 and T3, respectively. The difference in number arises from the asynchronous data gaps in the time series of the trenches, since rainfall events occurring during data gaps were not analysed. Each simple SSF event and subevent (see Section 2.3.4) was associated with a specific triggering rainfall event (see Section 2.3.5). Figure 5a gives an overview of the precipitation rates of these individual triggering rainfall events. Some SSF metrics (e.g. V_{tot}) were not calculated for subevents but only defined for simple and complex events. Figure 5b shows the intensities of the triggering rainfall events associated with simple SSF events and the averaged intensities of the triggering rainfall events belonging to the same complex SSF event. Thus, one intensity value (e.g. I_5) was assigned to each SSF event, whether simple or complex. As expected, the rates decreased from I_5 to I_m and were quite similar for the two trenches.

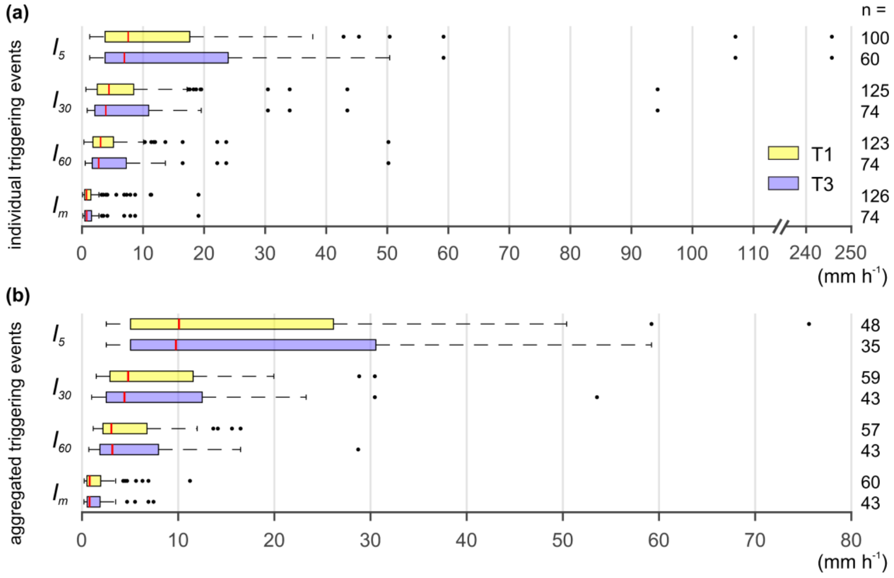

Figure 5. Overview of the rainfall rates of triggering rainfall events; (a) individual triggering events, (b) triggering events aggregated by their association with simple or complex SSF events (for complex SSF events, intensities are averaged within the group). The sample size (n) is shown on the right of each boxplot. I_5, I_{30} and I_{60} are the max. 5-, 30- and 60-min rates, respectively, and I_m is the mean rate.

The rainfall depths of triggering, ambiguous, and non-triggering events are shown in Figure 6a, while Figure 6b shows the total depth calculated by considering all rainfall events (triggering and, where present, ambiguous) associated with the same simple or complex SSF event. Most triggering events were larger than 5 mm; however, smaller events were also identified. T3 was characterized by larger triggering and non-triggering events, suggesting a higher precipitation threshold for the activation of SSF at the site. Moreover, at T3 the aggregated triggering and ambiguous events (Figure 6b) were usually characterized by a higher total rainfall amount compared to T1.

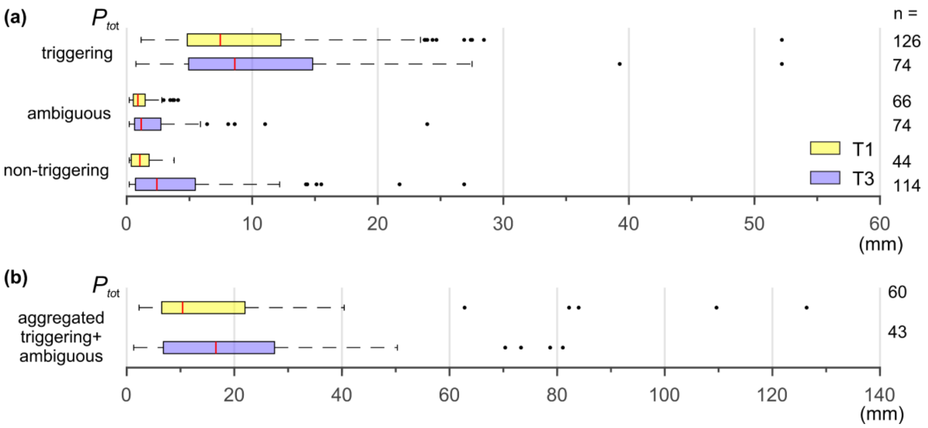

Figure 6. Overview of the (a) total rainfall depths of triggering, ambiguous and non-triggering rainfall events as well as of (b) total rainfall depth of the triggering and ambiguous rainfall events associated with each simple or complex SSF event (sum within each SSF event). The sample size (n) is shown on the right of each boxplot.

3.2 SSF events characteristics

In total, 38 simple events, 22 complex events and 88 subevents were identified at T1, whereas at T3, 29 simple events, 14 complex events and 45 subevents were identified. The characteristics of the analysed SSF events are presented in Figure 7. Overall, the SSF response was similar at the two sites. However, at T3 the 75th percentile of V_{tot}, $\bar{Q}$, MCA and $Q_{\Delta max}$ was higher, while it was longer for the response time and shorter for the lag time. Negative response times and lag times occur when the centroid of the rainfall event is located after the SSF start and peakflow time, respectively. The smaller response time at T1 indicates a faster SSF response and a smaller precipitation threshold, as the rainfall preceding the centroid was often sufficient to trigger SSF. The period between start of rainfall and start of SSF events (not plotted in Figure 7) was sometimes as small as 5 minutes at both sites (5 min time resolution).

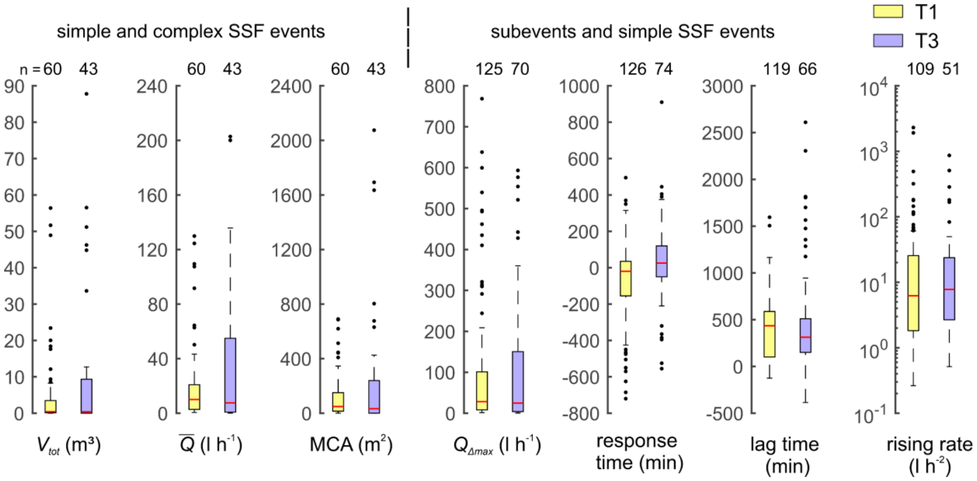

Figure 7. Overview of the characteristics of the analysed SSF events. The sample size (n) is shown above the boxplots.

3.3 Correlation Analysis

To study how different rainfall event characteristics and antecedent conditions influence the SSF response, the relationships between the descriptive metrics were analysed using the Spearman rank correlation (r_s). Figure 8 presents the resulting correlation matrix, with the correlations for T1 and T3 displayed in the upper right and lower left portions of the table (i.e. above and below the diagonal), respectively. The correlation patterns of T1 and T3 show a high level of congruence, suggesting that the observed relationships are not site specific. The total precipitation showed a moderate relationship with the intensities, with relationship strength increasing from I_m to I_{60}. The correlation between VWC$_i$ and Q_i was strong at both trenches. However, while at T1, due to the continuous baseflow, Q_i steadily increased with VWC$_i$ starting from small VWC$_i$ values, at T3 the increase started at higher VWC$_i$, since at this site baseflow was absent during dry conditions and thus lower VWC$_i$ (data not shown). Comparing the correlation of the composite variable P_{tot}+ASI and P_{tot} with the other metrics showed that for P_{tot}+ASI the correlation was sometimes smaller than for P_{tot}, suggesting that the influence of the initial soil moisture conditions (i.e. ASI) was overemphasized in the composite variable. We therefore also tested the composite variable P_{tot}+ASI$_{adj}$, where ASI was weighted (adjusted) in order to achieve maximum correlation (see Section 2.3.8). The variables V_{tot}, $\bar{Q}$, MCA and $Q_{\Delta max}$ showed a marked improvement in correlation when the composite variable with the weighted ASI was considered, indicating a strong influence of the initial conditions on these variables. At both trenches, the increase in correlation and the weighting factor were greater for MCA than for V_{tot} and $\bar{Q}$, suggesting that the initial conditions are even more relevant for MCA. The improvement in correlation and the weighting factor were higher at T3, indicating that antecedent conditions play a stronger role at that site than at T1. For example, for $Q_{\Delta max}$ the correlation increased by 0.46 at T3 but only by 0.07 at T1, and the weights for ASI were roughly two times higher for T3 than for T1. For the variables rising rate and response time, the differences in correlation with P_{tot} and P_{tot}+ASI$_{adj}$ were null or negligible, suggesting that initial conditions have little impact on these temporal metrics. Lag time was not correlated with P_{tot}, and the higher correlation obtained for the composite variable arise from its relatively higher correlation with VWC$_i$.

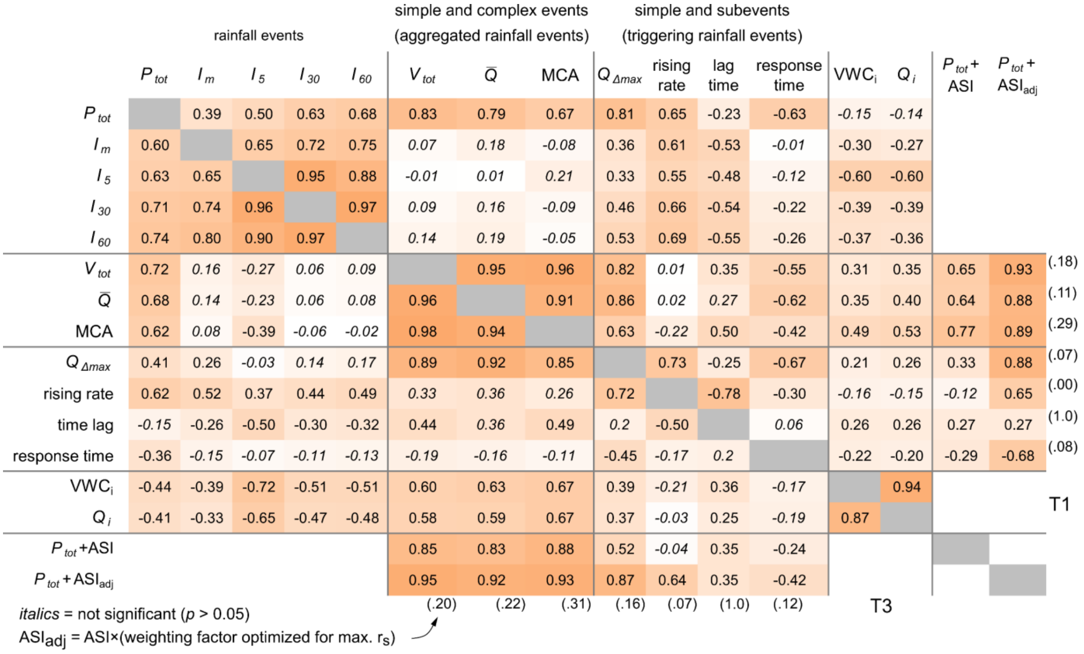

	rainfall events					simple and complex events (aggregated rainfall events)			simple and subevents (triggering rainfall events)								
	P_{tot}	I_m	I_5	I_{30}	I_{60}	V_{tot}	$\bar{Q}$	MCA	$Q_{\Delta max}$	rising rate	lag time	response time	VWC$_i$	Q_i	P_{tot}+ ASI	P_{tot}+ ASI$_{adj}$	
P_{tot}		0.39	0.50	0.63	0.68	0.83	0.79	0.67	0.81	0.65	-0.23	-0.63	*-0.15*	*-0.14*			
I_m	0.60		0.65	0.72	0.75	*0.07*	*0.18*	*-0.08*	0.36	0.61	-0.53	*-0.01*	-0.30	-0.27			
I_5	0.63	0.65		0.95	0.88	*-0.01*	*0.01*	*0.21*	0.33	0.55	-0.48	*-0.12*	-0.60	-0.60			
I_{30}	0.71	0.74	0.96		0.97	*0.09*	*0.16*	*-0.09*	0.46	0.66	-0.54	-0.22	-0.39	-0.39			
I_{60}	0.74	0.80	0.90	0.97		*0.14*	*0.19*	*-0.05*	0.53	0.69	-0.55	-0.26	-0.37	-0.36			
V_{tot}	0.72	*0.16*	*-0.27*	*0.06*	*0.09*		0.95	0.96	0.82	*0.01*	0.35	-0.55	0.31	0.35	0.65	0.93	(.18)
$\bar{Q}$	0.68	*0.14*	*-0.23*	*0.06*	*0.08*	0.96		0.91	0.86	*0.02*	*0.27*	-0.62	0.35	0.40	0.64	0.88	(.11)
MCA	0.62	*0.08*	-0.39	*-0.06*	*-0.02*	0.98	0.94		0.63	*-0.22*	0.50	-0.42	0.49	0.53	0.77	0.89	(.29)
$Q_{\Delta max}$	0.41	0.26	*-0.03*	*0.14*	*0.17*	0.89	0.92	0.85		0.73	-0.25	-0.67	0.21	0.26	0.33	0.88	(.07)
rising rate	0.62	0.52	0.37	0.44	0.49	*0.33*	*0.36*	*0.26*	0.72		-0.78	-0.30	*-0.16*	*-0.15*	*-0.12*	0.65	(.00)
time lag	*-0.15*	-0.26	-0.50	-0.30	-0.32	0.44	*0.36*	0.49	*0.2*	-0.50		*0.06*	0.26	0.26	0.27	0.27	(1.0)
response time	-0.36	*-0.15*	*-0.07*	*-0.11*	*-0.13*	*-0.19*	*-0.16*	*-0.11*	-0.45	*-0.17*	*0.2*		-0.22	-0.20	-0.29	-0.68	(.08)
VWC$_i$	-0.44	-0.39	-0.72	-0.51	-0.51	0.60	0.63	0.67	0.39	*-0.21*	0.36	*-0.17*		0.94			
Q_i	-0.41	-0.33	-0.65	-0.47	-0.48	0.58	0.59	0.67	0.37	*-0.03*	0.25	*-0.19*	0.87				T1
P_{tot}+ASI						0.85	0.83	0.88	0.52	*-0.04*	0.35	-0.24					
P_{tot}+ASI$_{adj}$						0.95	0.92	0.93	0.87	0.64	0.35	-0.42					
						(.20)	(.22)	(.31)	(.16)	(.07)	(1.0)	(.12)	T3				

italics = not significant ($p > 0.05$)
ASI$_{adj}$ = ASI×(weighting factor optimized for max. r_s)

Figure 8. Spearman rank correlation coefficients between antecedent conditions, rainfall and SSF event characteristics at T1 (above diagonal) and T3 (below diagonal)

3.3.1 Relationship between rainfall characteristics, total SSF Volume and Minimum Contributing Area (MCA)

For both trenches V_{tot} strongly correlated with P_{tot}, but the antecedent conditions also had a major influence on the SSF response. For similar P_{tot} the V_{tot} of events characterized by wet initial conditions were generally around one to three orders of magnitudes larger than their drier counterparts (see Figure 9 and Figure 10). Nevertheless, for very large events (P_{tot} > 40–50 mm) the influence of the antecedent conditions was often less pronounced and the P_{tot}–V_{tot} relationship was poor, as larger P_{tot}

did not always imply higher V_{tot}. Visual inspection of the scatterplots revealed that initial trenchflow (Q_i) was valuable to explain some of the results of T3, where events characterized by similar VWC$_i$ and P_{tot} generated different trenchflow amounts (e.g. events with P_{tot} 15–20 mm in Figure 10). The rainfall amount to trigger a SSF response was minimal (2–3 mm) for both trenches. Nevertheless, the generation of somewhat larger events (V_{tot} >100 l) required ca. 5 mm of rainfall for wet antecedent conditions and ca. 10 mm for dry ones at T1, whereas at T3 the amount was ca. 5 mm and ca. 25 mm, respectively. The influence of the antecedent conditions was effectively accounted for using P_{tot}+ASI$_{adj}$, as shown in Figure 11 and Figure 12, where for both trenches wet and dry events tend to form one common trend.

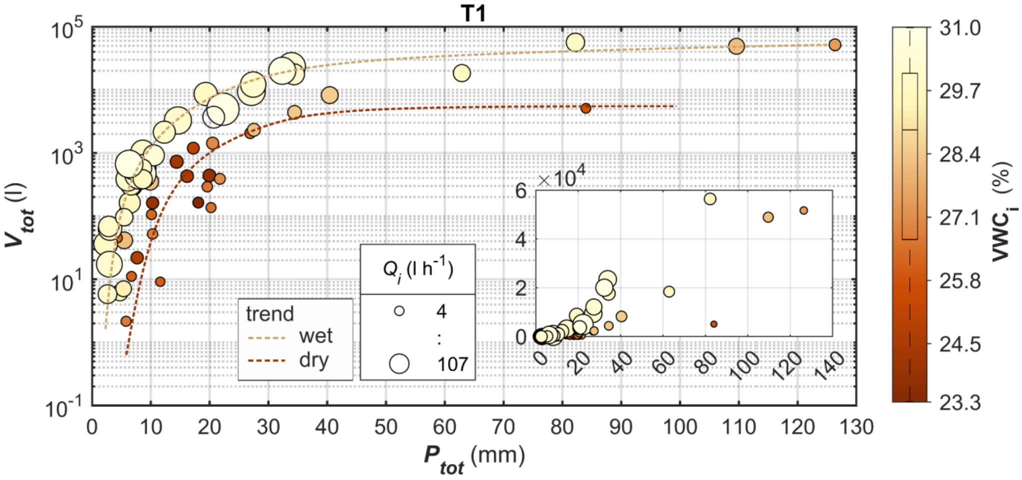

Figure 9. Total rainfall versus total SSF volume and antecedent conditions at T1 (event-based). The dashed lines (manually plotted) represent trends for wet and dry antecedent conditions. The insert shows the same data on a linear-linear scale. In the insert the marker size was reduced for better visualization. The antecedent conditions are represented by VWC$_i$ (colour of markers) and Q$_i$ (size of markers). The boxplot in the colorbar describes the distribution of VWC$_i$.

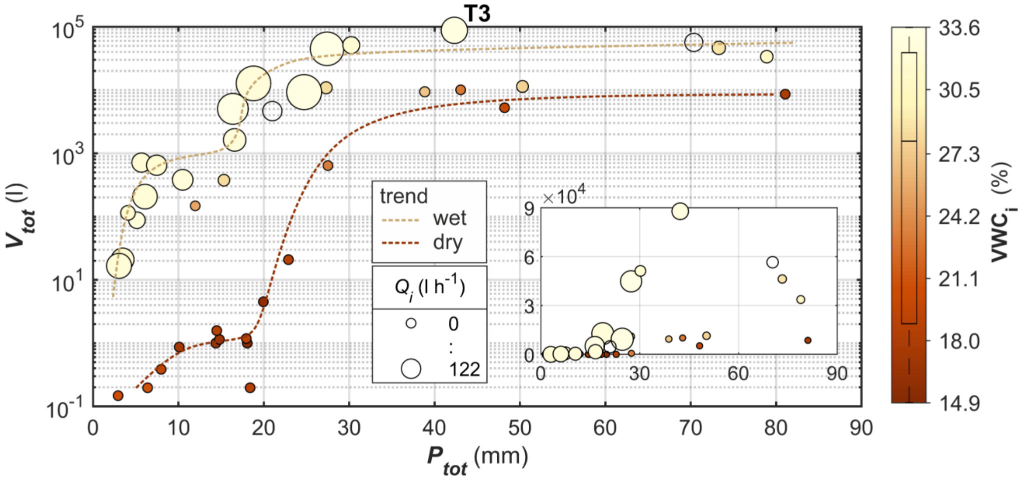

Figure 10. Total rainfall versus total SSF volume and antecedent conditions at T3 (event-based). The dashed lines (manually plotted) represent trends for wet and dry antecedent conditions. The insert shows the same data on a linear-linear scale. In the insert the marker size was reduced for better visualization. The antecedent conditions are represented by VWC$_i$ (colour of markers) and Q$_i$ (size of markers). The boxplot in the colorbar describes the distribution of VWC$_i$.

Overall, at T1 the V_{tot} steadily increased with P_{tot} without showing any significant change in slope (Pearson correlation coefficient = 0.87), whereas at T3 this relationship appeared to undergo different stages, resulting in something like a step function on the semi-logarithmic plot (Figure 9 and Figure 10).

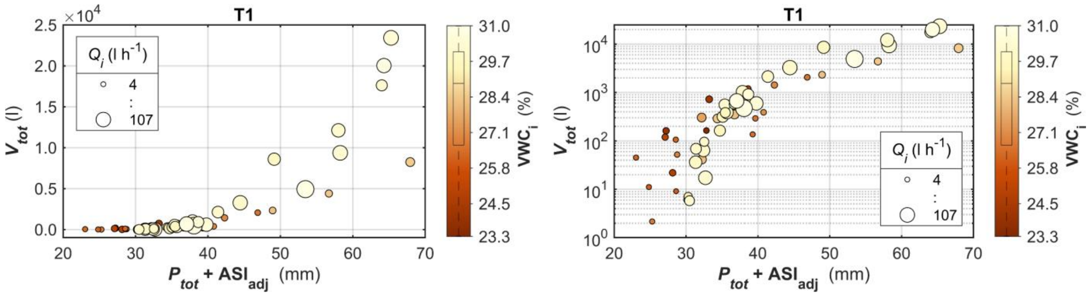

Figure 11. Relationship between total SSF volume and total rainfall + ASI$_{adj}$ at T1 (left plot is lin-lin and right plot is lin-log). The largest events are not included in the plots. The antecedent conditions are represented by VWC$_i$ (colour of markers) and Q$_i$ (size of markers). The boxplot in the colorbar describes the distribution of VWC$_i$.

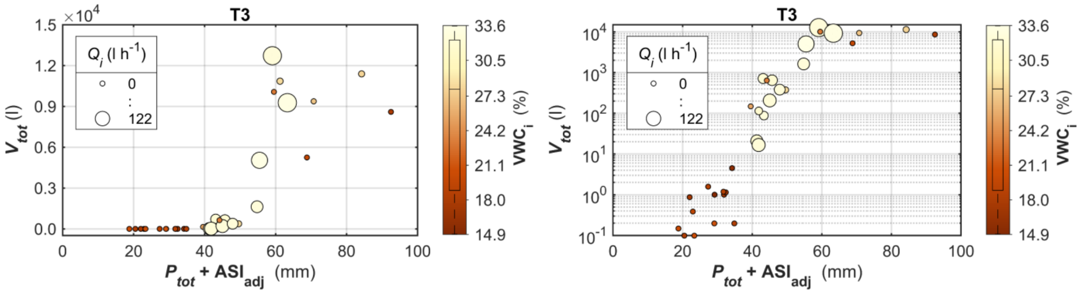

Figure 12. Relationship between total SSF volume and total rainfall + ASI$_{adj}$ at T3 (left plot is lin-lin and right plot is lin-log). The largest events are not included in the plots. The antecedent conditions are represented by VWC$_i$ (colour of markers) and Q$_i$ (size of markers). The boxplot in the colorbar describes the distribution of VWC$_i$.

The initial conditions strongly influenced MCA, as under dry conditions the area stayed relatively small, whereas under wet conditions the area generally increased with P_{tot} reaching a maximum of ca. 700 m² and 2000 m² at T1 and T3, respectively (Figure 13). The increase in MCA indicates an increase of the SSF contributing area and/or of the subsurface runoff coefficient (C_{sub}). Most likely, it is a combination of both, because if the largest observed MCA (i.e. 700 and 2000 m²) is assumed to be the contributing area for all events, the C_{sub} of medium to small events would be very small (e.g. 1–3% for events with $V_{tot} \approx$ 0.4 m³). At T3 the MCA increased steeply for events with P_{tot} greater than ca. 15 mm and wet initial conditions.

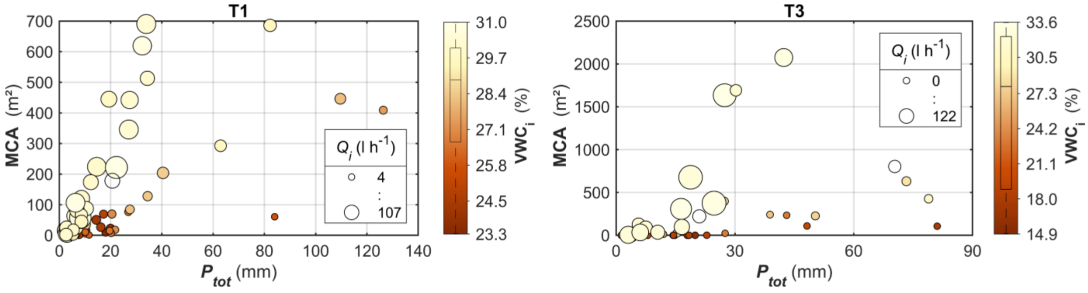

Figure 13. Relationship between MCA and total rainfall as well as antecedent conditions. The antecedent conditions are represented by VWC$_i$ (colour of markers) and Q$_i$ (size of markers). The boxplot in the colorbar describes the distribution of VWC$_i$.

To further analyse the relationship between V_{tot}, P_{tot}, MCA and VWC$_i$ the events were separated into two groups (wet and dry) based on their associated VWC$_i$. Furthermore, for T1 and T3 only events associated with $P_{tot} < 40$ mm and $P_{tot} = 15$–43 mm, respectively, were considered in the following analysis, as for those a more distinct V_{tot} vs P_{tot} relationship was identified. As shown in Figure 14, within the considered range of P_{tot}, the linear fit between V_{tot} and P_{tot} was good (at T1, r² was 0.89 for wet events and 0.58 for dry events, whereas for T3, r² was 0.92 and 0.54 for wet and dry events, respectively). Nevertheless, visually, especially for wet events of T1, the rate at which V_{tot} increases seems to rise with P_{tot}, suggesting that a quadratic function would be better suited to represent the observed trend. This trend indicates that the active contributing area and/or the subsurface runoff coefficient (C_{sub}) increases with P_{tot}, which is consistent with the linear increase in MCA with P_{tot} shown in Figure 13. The linear fit of MCA vs P_{tot} (Eq. 4) was used to derive V_{tot} by multiplying Eq. 4 by P_{tot} (Eq. 5) (see Section 2.3.8). Using the coefficients from the fitted Eq. 4 (see Table 3), the resulting Eq. 5 is plotted as a continuous line in Figure 14.

Table 3 Coefficients and r² of the fitted Eq. 4 and r² of Eq. 5.

Trench	Condition	*a*	*b*	r² (Eq. 4)	r² (Eq. 5)
T1	wet	18.9	-66.6	0.92	0.96
	dry	3.3	-12.0	0.38	0.68
T3	wet	76.5	-949	0.79	0.91
	dry	12.2	185	0.35	0.51

The results show that the observed V_{tot} –P_{tot} relationship can be explained by an increase in the contributing area and/or C_{sub} with P_{tot}. Furthermore, the very different quadratic coefficients (*a*) for wet and dry conditions suggest that initial soil moisture conditions strongly influence the rate at which the contributing area (or the C_{sub}) increases with P_{tot}.

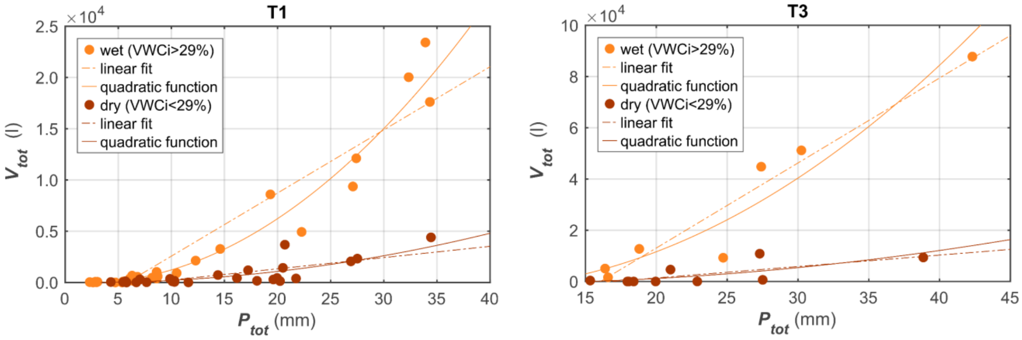

Figure 14. Total rainfall versus total SSF volume of events with dry and wet antecedent conditions, with the best linear fit (dash-dotted line) and quadratic function (Eq. 5) (solid line).

The quadratic coefficient (*a*), computed for wet events, is higher for T3 than for T1, indicating that at that site, once the threshold (15 mm) is exceeded, the actively contributing area increases faster with P_{tot}.

Rainfall intensities (I_5, I_{30}, I_{60} and I_m) showed a very poor and often not significant relationship with V_{tot} and MCA (Figure 8). For both SSF metrics the variation decreased with the intensity, such that small intensities were associated with extremely large as well as extremely small V_{tot} and MCA, and very large intensities were linked to relatively small V_{tot} and MCA. At T1 and T3, for example, the largest SSF volumes were associated to I_5 of merely 10 and 6 mm/h, respectively. The large V_{tot} and MCA can be explained by the large P_{tot} and high antecedent soil moisture content associated with the events. Both have to be high, as emphasized by the results at T1 where under similarly high P_{tot} (82–84 mm) the event with dry antecedent conditions generated only 9% of the volume of the event with wet antecedent conditions, despite having some of the highest recorded intensities (I_5 and I_{30} of 76 and 29 mm/h, respectively).

3.3.2 Peakflow

The Spearman's correlation analysis showed that the maximum increase in discharge ($Q_{\Delta max}$) was strongly correlated to V_{tot}, and consequently to P_{tot}, especially when the antecedent conditions were also taken into account using P_{tot}+ASI$_{adj}$ (Figure 8). Comparing the correlation with P_{tot} and P_{tot}+ASI$_{adj}$, the improvement in correlation was notably great for T3, suggesting a stronger influence of the initial conditions on $Q_{\Delta max}$ at that site.

The scatterplot analysis further showed how $Q_{\Delta max}$ was controlled by P_{tot} as well as antecedent soil moisture (VWCi) and initial flow (Q_i) mainly for events associated to rainfall events smaller than ca. 20 mm (Figure 15 and Figure 16). At T3, for example, 13–14 mm of precipitation with similar intensity resulted in a $Q_{\Delta max}$ of 1 l/h or ca. 230 l/h, depending on whether the initial conditions were dry or wet, respectively; and at T1, 15–16 mm of rainfall triggered a $Q_{\Delta max}$ of 6 l/h or more than 320 l/h based on the different initial conditions.

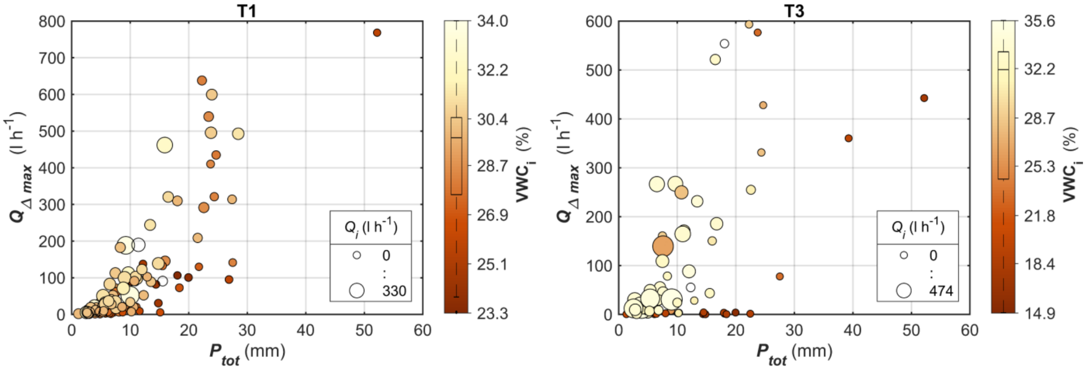

Figure 15. Relationship between $Q_{\Delta max}$ and P_{tot} as well as antecedent conditions. The antecedent conditions are represented by VWC$_i$ (colour of markers) and Q$_i$ (size of markers). The boxplot in the colorbar describes the distribution of VWC$_i$.

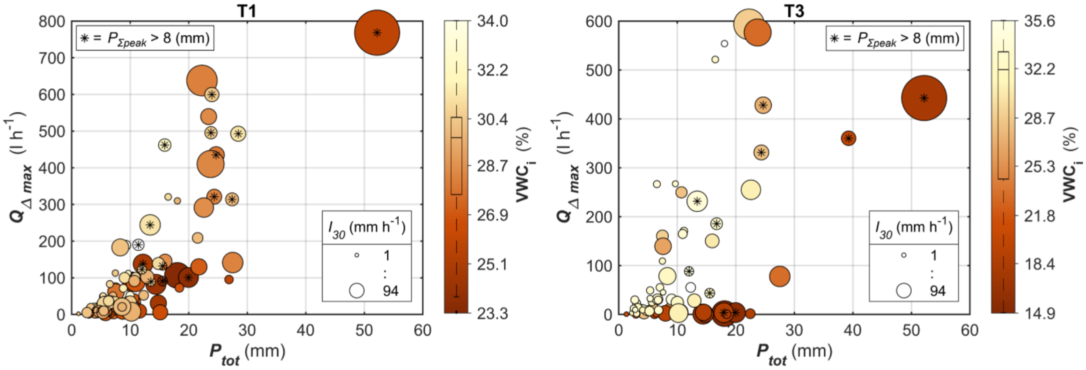

Figure 16. Relationship between $Q_{\Delta max}$ and P_{tot} as well as antecedent soil moisture conditions and I_{30}. Events were the cumulative rainfall calculated until peak rainfall intensity (I_5) is greater than 8 mm are marked with *. The size of the markers represents I_{30} and the colour of the markers represents the VWC$_i$. The boxplot in the colorbar describes the distribution of VWC$_i$.

For SSF events associated with larger rainfall events (P_{tot} > 20 mm), on the other hand, the initial conditions appeared to play a secondary role, as demonstrated by the extremely high $Q_{\Delta max}$ of events characterized by very dry initial conditions. For these larger events (P_{tot} > 20 mm) the rainfall intensity began to play a major role (Figure 16). However, this was not reflected by the results of the Spearman correlation analysis (Figure 8), as for the majority of events, which had P_{tot} < 20 mm, the intensity was not a controlling factor. At both trenches the highest $Q_{\Delta max}$ values were associated with fairly high rainfall intensities. For example, at T1 the largest $Q_{\Delta max}$ was associated with a rainfall intensity I_{30} of 94 mm/h (I_5 of 247 mm/h) and very dry initial conditions. Moreover, events with similar total rainfall of 22–23 mm and comparable initial conditions (moderately wet) exhibited a $Q_{\Delta max}$ ranging from 130 to 638 mm/h, which can be explained by an increase in intensity (from I_{30} 12 to 43 mm/h) associated with these events. Similarly, at T3, two events with P_{tot} of ca. 23 mm had $Q_{\Delta max}$ values of 250 and 580 l/h, explainable by the different associated rainfall intensities of 18 and 34 mm/h (I_{30}), respectively. The analysis also showed that the amount of rainfall preceding the peak 5-minutes rainfall intensity ($P_{\Sigma peak}$ in Figure 16) also played a role. At both trenches, high $Q_{\Delta max}$ values were associated with moderate intensities if $P_{\Sigma peak}$ was large. Hence, the rainfall structure (i.e. temporal distribution of rainfall intensities) also showed to influence the SSF response. The results suggest that a combination of large P_{tot} and high intensities was required to achieve very high $Q_{\Delta max}$, while initial conditions played a subordinate role.

3.3.3 Rising rate, lag time and response time

The rising rate was positively correlated to P_{tot} as well as rainfall rate (Figure 17). Especially events with extremely high rising rates were always associated with large P_{tot} and/or high rainfall intensities. Of the analysed intensities, I_{60} appeared to be the most suited to explain the differences in rising rates among events with similar P_{tot}, although I_{30} and I_m were also suitable. The influence of intensity was, for example, evident at T1, where events with a similar P_{tot} of 22–24 mm showed rising rates ranging from ca. 15 to 1900 l/h², which can be explained by the associated I_{60} ranging from 8 to 22 mm/h. The antecedent conditions, on the other hand, appeared to be less relevant. Nevertheless, some events with the highest rising rates were characterized by a low or a lack of initial trenchflow (see * in Figure 17), suggesting that dry antecedent conditions do not hinder high rising rates but sometimes favour them. This is evident in the results of T1, where for events with similar P_{tot}, those characterized by dry initial conditions often exhibited higher rising rates than those with wetter initial conditions. At T3, the influence of the initial conditions was less evident, partly due to the smaller number of events with dry initial conditions (see boxplots in Figure 17), as some events were excluded from the rising rate analysis (based on the criterion $Q_{\Delta max}$ > 3 l/h, see Section 2.3.6).

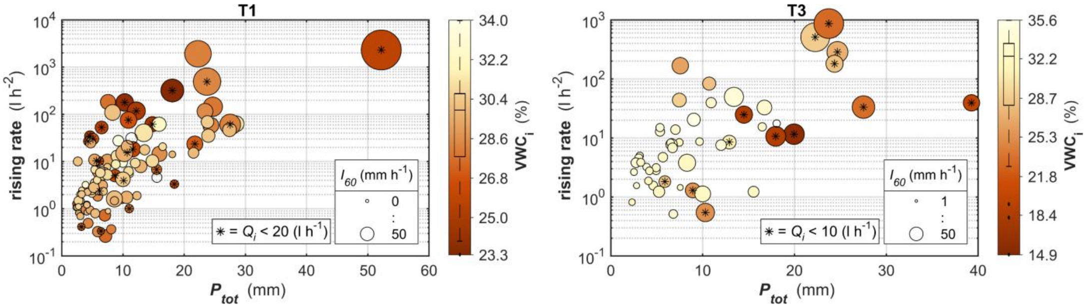

Figure 17. Relationship between rising rate and P_{tot} as well as antecedent conditions and I_{60}. The size of the markers represents I_{60} and the colour of the markers represents the VWC$_i$. Events with Q_i < 20 l/h are marked with *. The boxplot in the colorbar describes the distribution of VWC$_i$.

The time between centroid rainfall and peak flow (i.e. lag time) greatly varied for events with small rising rates, whereas it was mostly short for events with a high rising rate (Figure 18). For example, the median lag time of events with a rising rate larger than 50 l/h² was 20 min (T1) and 85 min (T3), whereas it was 465 min (T1) and 328 min (T3) for smaller rising rates.

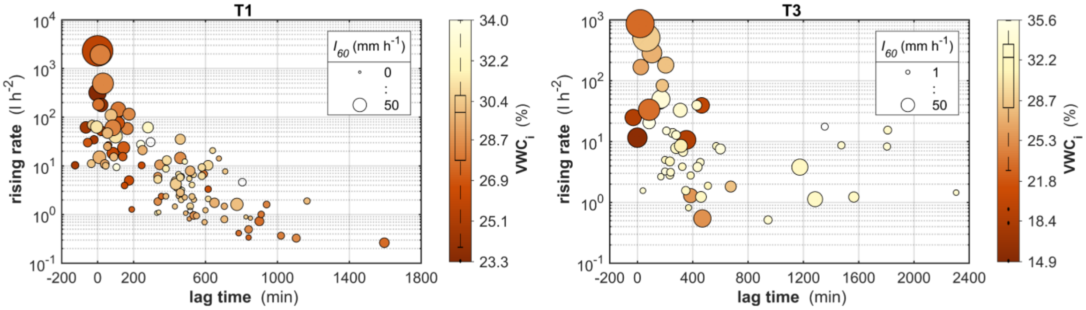

Figure 18. Relationship between rising rate and lag time as well as antecedent conditions and I_{60}. The size of the markers represents I_{60} and the colour of the markers represents the VWC$_i$. The boxplot in the colorbar describes the distribution of VWC$_i$.

The lag time was not sensitive to the size of the rainfall event (P_{tot}) but was sensitive to its intensity (I_5 to I_m). Greater intensities were associated with smaller lag times. For example, at T1 the median I_{60} of events with a lag time greater than 100 min was

2.4 mm/h, whereas for shorter lag times it was 6.6 mm/h. Similarly, at T3 the median I_{60} was 2.5 and 6.5 mm/h, respectively. Dry initial conditions also seem to favour short lag times, as events with dry antecedent conditions generally exhibited short lag times. For example, at T1 the median lag time of events characterized by VWCi and Q_i smaller than 26 % and 20 l/h was 20 min and 7 min, respectively, whereas for larger VWCi and Q_i it was 460 min and 490 min, respectively. T3 showed a similar pattern: the difference in the median lag time of events with VWCi and Q_i smaller and larger than 26 % and 10 l/h, respectively, was 213 min and 200 min, respectively.

The time between rainfall and SSF start can be calculated considering the rainfall centroid (i.e. response time, which is used in this analysis) as well as the start of the rainfall event. For both cases, their relationship to the rainfall event characteristics was found to be comparable. The P_{tot} as well as the cumulative rainfall calculated up to the SSF start showed to have a poor influence on the response time. Nevertheless, considering the cumulative rainfall up to SSF start, higher rainfall amounts were associated to a smaller variance in response time. Similar results were observed for the rainfall intensities preceding the SSF start, with variance decreasing as the intensities increase. These results indicate that a quick SSF response is more likely triggered by short, intense, and temporally focused rainfall events. The antecedent conditions did not show a clear relationship with the response time. Overall, the relationship between response time, rainfall event characteristics and antecedent conditions were not well defined.

3.3.4 Seasonality

To study the seasonality, the SSF and rainfall events were divided by season. For selected metrics the trimmed mean (i.e mean computed after excluding the lowest and highest 10% of values) was calculated on a seasonal basis (see Figure 19); thus, the largest outliers were not considered. The VWC_i and I_{30} associated to simple and complex events as well as non-triggering rainfall events showed the same seasonal distribution as for the simple events and subevents and are thus not shown in Figure 19. Overall, both trenches showed similar seasonal patterns. The V_{tot} and MCA were notably higher in winter and spring. This is clearly linked to the higher VWC_i of these seasons, as less water is required to refill the subsurface storage. The P_{tot} was higher in spring than winter. Nevertheless, the higher winter VWC_i seems to compensate for the smaller rainfall amounts. The larger $^*P_{tot}$ (i.e. P_{tot} of aggregated events) at T1 is the result of the longer duration of the SSF events and thus a larger number of aggregated rainfall events. High $Q_{\Delta max}$ were observed in spring at both trenches and at T1 it was also relatively high during fall and summer. The on average low $Q_{\Delta max}$ observed during the summer months at T3, despite the occurrence of large and intense rainfall events, can be explained by the dry initial conditions and their stronger influence on the SSF response at this site. The rising rate was highest in spring at T3 and in summer at T1. The longest lag time was observed in spring at both trenches, and arises due to a handful of events with extremely long lag time.

The total rainfall of non-triggering rainfall events ($^{**}P_{tot}$ in Figure 19) also shows a seasonal trend. The highest and lowest $^{**}P_{tot}$, observed during summer and winter months, respectively, can be explained by the VWC_i as well as the change in interception storage (i.e. leafed and leafless periods). The same picture is given when the events are divided by dormant (November–April) and growing season (May–October). Overall, the interception storage appears to be small with ca. < 2–3 mm and seems to play a subordinate role in controlling the SSF response in the studied areas.

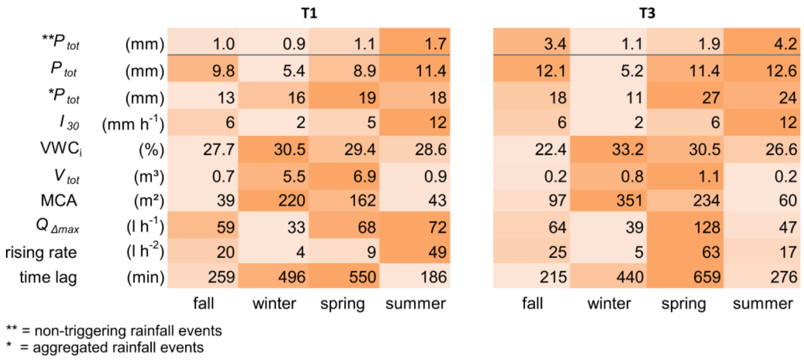

		T1				T3			
		fall	winter	spring	summer	fall	winter	spring	summer
$^{**}P_{tot}$	(mm)	1.0	0.9	1.1	1.7	3.4	1.1	1.9	4.2
P_{tot}	(mm)	9.8	5.4	8.9	11.4	12.1	5.2	11.4	12.6
$^{*}P_{tot}$	(mm)	13	16	19	18	18	11	27	24
I_{30}	(mm h^{-1})	6	2	5	12	6	2	6	12
VWC$_i$	(%)	27.7	30.5	29.4	28.6	22.4	33.2	30.5	26.6
V_{tot}	(m³)	0.7	5.5	6.9	0.9	0.2	0.8	1.1	0.2
MCA	(m²)	39	220	162	43	97	351	234	60
$Q_{\Delta max}$	(l h^{-1})	59	33	68	72	64	39	128	47
rising rate	(l h^{-2})	20	4	9	49	25	5	63	17
time lag	(min)	259	496	550	186	215	440	659	276

** = non-triggering rainfall events
* = aggregated rainfall events

Figure 19. Seasonality of SSF and rainfall events characteristics

4 Discussion

4.1 Influence of total rainfall and antecedent conditions on contributing area and subsurface stormflow generation

The analysis has shown that at both trenches the event SSF volume (V_{tot}) is controlled by rainfall amount (P_{tot}) and antecedent wetness conditions (VWC$_i$ and Q_i), with wet conditions producing one to three orders of magnitude larger events (V_{tot}) under similar P_{tot} (Figure 9 and Figure 10). To account for the influence of the initial conditions on the generated stormflow volume, different authors have used the composite metric P_{tot}+ASI, which allowed to improve correlation strength and threshold detection (e.g. Detty and McGuire, 2010; Fu et al., 2013; Han et al., 2020; Zwartendijk et al., 2023). Nevertheless, ASI can over- or under-represent the initial soil moisture conditions in the composite metric P_{tot}+ASI, as it is highly dependent on the depth of the considered soil moisture profile; for the same soil moisture content, deeper profiles will yield higher ASI values, while shallower ones yield lower values. Therefore, as shown by Fu et al. (2013), the optimum depth to obtain the best fit can be site dependent. Hence, in this study we weighted the initially computed ASI in order to obtain the best fit to the datasets. The observed higher correlation of V_{tot} vs P_{tot}+ASI$_{adj}$ than vs P_{tot} highlights the considerable influence of the initial conditions on the total flow, and shows that the storage deficit, linked to drier antecedent conditions, was effectively accounted for using ASI$_{adj}$ (see Figure 8). The correlation increased by 0.1 at T1 and by 0.2 at T3. The larger increase in correlation and the slightly higher weight at T3 indicates that the initial conditions have a higher influence at that site. This is also suggested by the on average larger rainfall amounts of the non-triggering rainfall events observed at T3 (Figure 6).

Despite the importance of the antecedent conditions for SSF events associated with small to medium P_{tot}, the data shows that for SSF events associated with very large total rainfall depths (P_{tot} > 40–50 mm) the influence of the antecedent conditions is often less pronounced and the P_{tot} –V_{tot} relationship is poor. These SSF events are characterized by a longer duration (> 75th percentile) and multiple peaks (subevents). Thus, the subsurface has time to drain between peaks and more water is lost by the consecutive rainfall events to replenish the storage deficit and during the transmission to the trench. The higher losses and inadequacy of considering only the wetness conditions at the start of these events are also reflected by the comparatively smaller MCA (Figure 13) and poorer P_{tot}+ASI$_{adj}$ vs V_{tot} relationship. These results show the limitation of the applied approach for extremely large, long multi-peak SSF events. This finding matches the observations of Tromp-van Meerveld and McDonnell (2006a) where a poorer P_{tot} –V_{tot} relationship and a weaker influence of the initial conditions is seen for SSF events associated to P_{tot} > 55 mm. Hrnčíř et al. also reported that for extremely large rainfall amounts (> 70 mm) the initial conditions only exerted a smaller control on the total subsurface stormflow.

Regarding smaller events, at both trenches, the minimum P_{tot} to trigger a SSF response under wet antecedent conditions was minimal, ranging between 2 and 3 mm, and was only slightly higher for dry antecedent conditions (Figure 9 and Figure 10). The results show that, although the initial conditions greatly influence V_{tot}, they are less relevant concerning the activation of

SSF. Other hillslope-based studies have also shown that small P_{tot} (<5–12 mm) are sufficient to activate SSF (e.g. Fu et al., 2013; Tromp-van Meerveld and McDonnell, 2006) and that, although wet antecedent conditions favour SSF activation and generate larger volumes, small P_{tot} are in some cases also sufficient to produce SSF under dry conditions (Noguchi et al., 2001).

At T1, beyond the SSF activation threshold of P_{tot} = ca. 2 mm, especially events associated with wet antecedent conditions, show a nearly linear increase in V_{tot} with P_{tot}. A similar linear increase, without any apparent further thresholds, was also observed at the catchment scale by Penna et al. (2011). In contrast, T3 is characterized by a sharp increase of V_{tot} with P_{tot} at ca. 15 mm and ca. 20 mm for wet and dry initial conditions, respectively (Figure 10 and Figure 11). These rainfall amounts represent a second threshold beyond which significantly more SSF is generated. The observations at T3 match the results of most SSF studies (e.g. Du et al., 2016; Fu et al., 2013; Tani, 1997; Tromp-van Meerveld and McDonnell, 2006), where such a sharp increase in V_{tot} was also observed. In the literature, the reported size of this second threshold, for the generation of significant SSF, under wet antecedent conditions ranges between 18–60 mm (Du et al., 2016; Mosley, 1979; Uchida et al., 2005; Weiler et al., 2006). Hence, our threshold of ca. 15 mm is located at the lower end of the spectrum of the reported values. Considering the composite variable P_{tot}+ASI$_{adj}$, the second threshold was at ca. 40 mm at T3 (Figure 11). Hence, given the P_{tot} thresholds of 15 mm (wet conditions) and 20 mm (dry conditions), the initial soil moisture accounted for 25 and 20 mm of water in the composite variable for wet and dry initial conditions, respectively.

The initial conditions also influenced the MCA, as for similar P_{tot} the MCA was generally higher under wet antecedent conditions (Figure 13). The linear correlation observed between MCA and P_{tot} (for P_{tot} < 40 mm at T1 and P_{tot} = 15–43 mm at T3), which was especially strong and exhibited a steeper slope for events with wet initial conditions, translates into a non-linear (quadratic) V_{tot}–P_{tot} relationship (see Eq. 4–5 in Section 2.3.8 and Figure 14), suggesting an increase in the contributing area and/or C_{sub} with P_{tot}. The increase of the contributing area with P_{tot} is backed by field observations, which indicate that the contributing area can be much smaller than the maximum MCA. For some smaller events at T1 and T3, the uppermost instrumented well located roughly 20 m above the trench did not show any reaction (i.e. no increase in water level), implying that for these cases the contributing area must have ended downslope of the well and was therefore smaller than the calculated maximum MCA. The increase in contributing area with storm size and wet antecedent conditions is in agreement with other studies at the hillslope scale (e.g. Šanda and Císlerová, 2009; Tromp-van Meerveld and McDonnell, 2006b, a) as well as at the catchment scale (e.g. Detty and McGuire, 2010; Zwartendijk et al., 2023). The dynamic nature of the subsurface contributing area and the difficulty to assess it, implies that converting the volumetric (hillslope) discharge into specific discharge (i.e. mm), which requires the use of a fixed area, can lead to unrepresentative and misleading specific discharge values. Hence, in this study, the volumes were not converted into mm.

Our findings support that, for small events, especially if characterized by dry antecedent conditions, the contributing area tends to be small, as an expansion further upslope is likely obstructed by transmission losses (i.e. leakage through the impeding layer) and/or storage deficits (i.e. "storage barriers"), which are overcome during larger precipitation events. Studies have shown that these storage barriers can result, among other factors, from the spatial variation of soil thickness, the topography of the impeding layer (i.e. depression storage) and the vertical variation in hydraulic conductivity, which controls the leakage rate through the impeding layer as well as the possible onset of faster lateral flow within upper more permeable layers (McGuire et al., 2024). Moreover, low soil moisture levels represent an additional barrier that needs to be overcome (Penna et al., 2011). These barriers can increase gradually or abruptly, as suggested by the gradual and sharp increase of V_{tot} as well as MCA with P_{tot} observed at T1 and T3, respectively (Figure 9, Figure 10 and Figure 13). At T3 a large observed storage barrier of ca. 10 mm prevents the further expansion of the contributing area (or C_{sub}) resulting in a phase of markedly reduced increase of V_{tot} with P_{tot} (Figure 10). At the site, this barrier, which is present during wet and dry initial conditions, is likely the result of depressions on the irregular bedrock topography, which have to be filled before any significant later flow originating from areas further upslope can occur (fill and spill mechanism). This is supported by the steep topography and spatial distribution of the outcrops observed in the field. Nevertheless, other mechanisms cannot be ruled out. At T1 the continuous baseflow and shallow water table suggest that at the site SSF is generated by the water table rising into a more permeable zone near the surface (transmissivity feedback mechanism). Thus, the gradual increase of V_{tot} with P_{tot} can be explained by a gradual increase in storage losses and/or vertical losses further upslope.

4.2 Controls on peakflow

Our results show that $Q_{\Delta max}$ is mainly controlled by P_{tot} and antecedent soil moisture conditions (VWCi) for events associated with rainfall events smaller than approximately 20 mm (Figure 15). Whereas for larger amounts of rainfall, while P_{tot} is still important, the initial conditions play a subordinate role and the rainfall intensity appears to be one of the main controlling factors. The switch from initial conditions to rainfall intensities as main controlling factor is not abrupt but gradual, especially at T1 where the influence of the initial conditions is less pronounced than at T3. The strong influence of the initial conditions on $Q_{\Delta max}$ is reflected by the increase in correlation when ASI_{adj} is added to P_{tot} (see Figure 8). The increase and the adjustment factor of ASI (i.e. weight of the ASI) are particularly high at T3, supporting the larger influence of the initial conditions at the site. The relatively weak (T1) and extremely weak (T3) correlation coefficients between $Q_{\Delta max}$ and the rainfall intensities confirm that the intensities alone are not sufficient to explain $Q_{\Delta max}$. The somewhat higher values observed for T1 can be explained by the combined effect of the higher V_{tot}–P_{tot} correlation and the correlation present between P_{tot} and the rainfall intensities. Moreover, at T1 the smaller influence of the antecedent soil moisture conditions suggests a smaller soil moisture storage, which being more easily filled up allows the rainfall intensity to exert a larger influence. Our analysis also shows that the amount of rainfall preceding the peak 5-minutes rainfall intensity ($P_{\Sigma peak}$ in Figure 16) plays a role, as moderate intensities produced high $Q_{\Delta max}$ when $P_{\Sigma peak}$ was large. The stronger influence of the initial conditions observed for smaller rainfall events can be explained by the larger fraction of water lost to fill the storage deficit of the soil and to expand the subsurface contributing area. Only when the storage is filled and the area is large are higher rainfall rates able to generate and sustain higher subsurface flowrates, and thus exert a larger control on $Q_{\Delta max}$. This is also backed by the higher $Q_{\Delta max}$ generated by events with moderate I_{30} but high precipitation amounts preceding peak rainfall.

Other authors observed similar relationships between peakflow, storm size, rainfall intensities and antecedent conditions. Noguchi et al. (2001) documented an increase in subsurface peakflow with I_{30} for events with wet conditions, while during dry conditions the relationship was less strong and only present for part of the observed trenchface. Hrnčíř et al. (2010) also found that the initial soil moisture had a major control on the subsurface peakflow. Moreover, Fu et al. (2013) observed that beyond a threshold of I_{30} of ca. 6 and 12 mm/h (two trenches) the I_{30} correlated to the subsurface peakflow. However, two events with large antecedent soil moisture conditions showed high peakflows even with low I_{30} (below threshold). At the catchment scale, Zwartendijk et al. (2023) observed how peakflow was highly correlated to P_{tot}+ASI as well as with V_{tot} and that while peakflow was also influenced by I_{60} the P_{tot} and antecedent conditions where the major controlling factors. These studies suggest that, like at our trench sites, rainfall intensity has a lower influence under dry initial conditions but once the storage deficit is filled and the contributing area is large high rainfall intensities can generate high trenchflows especially when associated with large P_{tot}.

4.3 Timing and rising rate

Our findings show how the rising rate is positively correlated to P_{tot} as well as rainfall rate (I_m, I_5, I_{30} and I_{60}) (Figure 17 and Figure 8). The relationship with P_{tot} is roughly exponential, although the scatter is relatively large in part due to the different rainfall intensities. Dry initial conditions seem to not hinder the generation of steep rising limbs but, in some instances, to favour it (observed at T1 but not at T3).

The lag time (centroid rainfall–peakflow) is short for events with high rising rates but greatly varies for events with lower rising rates, resulting in a negative correlation between rising rate and lag time (Figure 8 and Figure 18). Similar results were found when the time between peak rainfall and peakflow was considered. The link between short lag times and steep rising limbs suggest that short travel times reduce the dispersion of the rainfall pulse traveling through the subsurface allowing for a sharper increase in discharge.

The lag time was found to be not correlated to the size of the rainfall event but to its intensity. The correlation between lag time and intensities is negative (see Figure 8), with the lag time variability decreasing as rainfall intensities increase. For example, at T1 and T3 events with I_{30} exceeding 15 mm/h had a standard deviation of the lag time seven and four times smaller than events with lower intensity, respectively. At the catchment scale, similar observations were made by Zhang et at. (2021). Knapp et al. (2025), also found that the lag time was shortened by higher precipitation intensities and was largely unaffected by antecedent wetness conditions. Our observations also align with the findings of Han et al. (2020), as they report that the time required to generate connectivity in the hillslope-riparian-stream system, and hence produce significant runoff, was related to the peak rainfall intensity (I_{30}), but not the accumulated rainfall amount. Moreover, they observed how dry initial conditions can favour connectivity within the catchment. In agreement, we found that short lag times were often associated with dry initial conditions. Shorter lag times were also associated with smaller MCA (Figure 8), especially under dry antecedent conditions. Similarly, Haga et al. (2005) observed how, at the catchment scale, the lag time increased with the increasing source area.

Our results suggest that dry conditions can favour preferential flow, which allows the pulse to travel more quickly through the subsurface bypassing the dry matrix. Evidence of preferential flow in our study catchment was found by Pyschik and Weiler (2025). Furthermore, dry conditions were linked to smaller MCA and thus shorter flow paths, which in turn promote a shorter travel time and hence smaller lag times. The reduced lag time linked to higher intensities can also be explained by the associated faster wetting (assuming rainfall intensity < infiltration capacity) and thus a quicker arrival of the main rainfall pulse to the trench.

The response time (centroid rainfall–start SSF) showed to be poorly related to P_{tot} as well as to the cumulative rainfall calculated up to the start of the SSF event. Nevertheless, the variability in response time shows a decrease with increasing rainfall amounts preceding the SSF start. Similarly, higher rainfall intensities were associated with a lower variance in response time. Overall, the relationship between response time, rainfall event characteristics and antecedent conditions is not well defined. One of the causes is that a fast SSF response can be expected for small rainfall rates and amounts if the antecedent conditions are wet as well as for large and intense rainfalls if the conditions are dry. The timing of SSF can be controlled by a multitude of factors (e.g. soil depth, bedrock topography, macropore network, slope, permeability contrast etc.) whose relevance can change depending on antecedent conditions, rainfall characteristics and SSF-producing mechanism (e.g. saturated flow over impeding layer, macropore flow, flow in higher permeability zone) (McGuire et al., 2024). Besides these complexities, the way the response time is defined can also lead to a large variation in response times. For example, the time can be calculated from the centroid or the peak rainfall, which in turn are influenced by the method and thresholds (e.g. MIT 6 h) used to define the rainfall events, but also by the particular structure of the rainfall events. Using the start of the rainfall event is also problematic, as the time will be highly influenced by the rainfall structure. The result is that only a handful of authors have studied the response time and its relationship with rainfall as well as hillslope/catchment characteristics. The large range in the response time and its variability within the hillslope was documented by Freer et al. (2002), who, for example, described how a certain trench section responded ca. 4 times slower than the fastest one. An even higher variability was found at the catchment scale in the study of Zwartendijk et al. (2023), who also observed that the response time (start rainfall to start stormflow) was poorly to not significantly correlated to the antecedent conditions.

4.4 Seasonal variation of SSF

The results showed a marked seasonal variation of the SSF response (Figure 19). The observed pattern can be linked to the seasonal variation of the rainfall characteristics and antecedent conditions, which ultimately control the SSF response. For instance, the great V_{tot} and MCA in winter and spring can be explained by the combined high precipitation amounts and wet initial conditions. Similarly, at the catchment scale, Penna et al. (2015) reported a strong seasonal variability in runoff responses related to antecedent moisture conditions and rainfall event size, with runoff coefficients being markedly higher in summer than in spring. Sidle et al. (1995) documented greater runoff coefficients during the wet season, which in combination with larger precipitation events, produced greater SSF volumes at the hillslope scale. Likewise, Tromp-van Meerveld and McDonnell (2006a) reported greater trenchflow runoff coefficients in winter than in summer. Blume et al. (2009) observed shorter response times for streamflow in summer compared to winter, consistent with our findings of much smaller lag times in summer compared to the wetter winter and spring.

Given the relevance of the antecedent wetness conditions, many SSF studies simply divide the dataset into wet and dry periods or into growing (typically dry) and dormant seasons (typically wet) (e.g. Detty and McGuire, 2010; Sidle et al., 1995). Only a few studies, however, explicitly examine the seasonal variability of SSF, as most of them are based on short observation periods and thus only cover a limited number of events. Our study highlights the importance of investigating SSF over extended time periods in order to capture the responses across seasons and, ultimately, a wide range of rainfall characteristics and antecedent conditions.

5 Conclusions

Subsurface stormflow (SSF) volume was primarily controlled by total rainfall and antecedent wetness conditions, with wet initial conditions yielding up to three orders of magnitude more volume. At one of the two analysed trenched hillslopes, the volume increased gradually with rainfall, whereas at the other, the volume increased sharply beyond a specific precipitation threshold, which differed for dry and wet initial conditions. Our data suggests, that the observed increase of volume with rainfall is the result of an increase in the contributing area and/or subsurface runoff coefficient. Peakflow was mainly controlled by total rainfall and initial wetness conditions for small rainfall events, whereas for larger events the influence of the initial conditions diminished, and rainfall intensity as well as rainstorm structure became more dominant controlling factors. Steep rising limbs were related with short response times and occurred under higher rainfall amounts and intensities. Using a weighted antecedent soil moisture index (ASI) in the combined variable total rainfall+ASI helped to quantify the influence of initial soil moisture conditions relative to the total rainfall on the different SSF response metrics.

Our results highlight the complex interactions between rainfall characteristics, antecedent wetness conditions and SSF responses, which could only be captured by analysing many events across seasons, underscoring the importance of long observation periods. The rapid SSF response and the large volumes and flow rates observed at our 11–14 m wide trenches, coupled with their proximity to the stream, suggest that SSF can substantially contribute to streamflow. Thus, our findings can serve both as a benchmark to verify hillslope-scale hydrological models and as a proxy for predicting the occurrence and magnitude of SSF in catchment-scale models. Further studies at the trench sites focusing on the inter-event dynamics of soil moisture, water level, trenchflow and its partitioning as well as artificial rainfall experiments will help to shed more light on the complex processes controlling SSF at the hillslope scale.

6 Appendix A

The volumetric water content (VWC) was derived from the dielectric permittivity and temperature data using the Complex Refraction Index Model (CRIM) (Eq. A1) which accounts for the individual permittivities of air (K_{air}), solid (K_s) and water (K_{water}) (Roth et al., 1990). In the equation, K_a is the measured (apparent) dielectric permittivity while n and β are the porosity and shape factor, respectively.

$$\text{VWC} = 100 \times \frac{K_a^{\beta} - (1-n) \times K_s^{\beta} - nK_{air}^{\beta}}{K_{water}\,(T)^{\beta} - K_{air}^{\beta}} \tag{A1}$$

While the effect of temperature on K_{air} and K_s is negligible, on K_{water} it is not (Wraith and Or, 1999). Therefore, if temperature is not accounted for when calculating the VWC (e.g. using the Topp equation; Topp et al., 1980), diurnal temperature cycles and seasonal temperature variations can lead to erroneous VWC values. This was avoided by applying the CRIM with a temperature-corrected K_{water}. The temperature dependence of K_{water} was taken into account using Eq. A2 (Weast, R.C, 1986); where $T°$ is the temperature in degree Celsius.

$$K_{water} = 78.54 \times [1 - 4.579 \times 10^{-3}(T° - 25) + 1.19 \times 10^{-5}(T° - 25)^2 - 2.8 \times 10^{-8}(T° - 25)^2] \tag{A2}$$

Nevertheless, an accurate temperature-corrected VWC can only be obtained if the CRIM-variables porosity (n) and K_s are reasonably well known, as those variables have a considerable influence on the resulting VWC. Hence, by applying the CRIM the temperature effect can be accounted for but the uncertainty on the absolute VWC values is related to the uncertainty of K_s and, more importantly, porosity (n).

In this study, K_s was assumed to be 4, since for mineral soils it typically ranges between 3 and 5 (Behari, 2005; Chan and Knight, 1999; Kirsch, 2009). A β of 0.5 was used, as this is the most commonly used value (Zadhoush et al., 2021), and K_{air} was set to 1. Where available, the porosity measured in the lab (from fitted water retention curve obtained from HYPROP 2 and WP4C (METER-Group) measurements) for the undisturbed soil samples taken near the sensor location was considered. However, soil samples were only collected along the deepest soil moisture profile (B3), thus for the shallower profiles (B1 and B2) the porosities were estimated based on the one measured at B3. The lab-measured porosities were adjusted when the VWC calculated with the CRIM was much lower than the one obtained using the Topp equation. The maximum observed VWC derived from the Topp equation was used as a guideline to adjust and estimate the porosity, under the assumption that during saturated or near-saturated conditions the VWC approximates porosity. The porosities used for the final calculation are shown in Table A1.

Table A1. Porosity at the sensor's location used to calculate the soil moisture (CRIM)

T1				T3			
	B1	B2	B3		B1	B2	B3
depth (m BGL)	porosity (-)	porosity (-)	porosity (-)	depth (m BGL)	porosity (-)	porosity (-)	porosity (-)
0.1	0.57	0.57	0.57*	0.1	0.54	0.54	0.54*
0.3	0.52	0.52	0.52*	0.3	0.51	0.51	0.51*
0.6	0.42	0.45	0.34*	0.6	0.55	0.52	0.52*
1.5			0.32	1.0			0.42
2.0			0.42	1.5			0.36 (0.29*)
2.5			0.42	2.0			0.41 (0.25*)

* = lab-measured porosities
(not used porosity)

7 Appendix B

The SSF events were delineated using a semi-automatic method developed within this study. In the following, the method is described in detail, including inputs, outputs, implemented steps and variables involved.

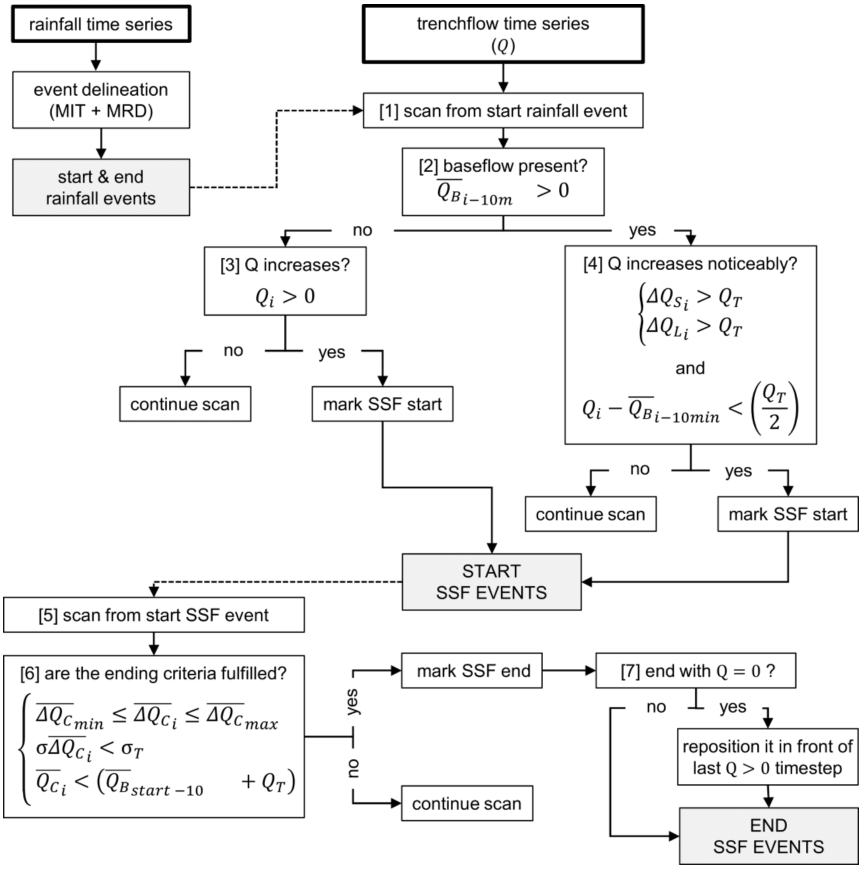

Figure B1. Flow chart of the subsurface stormflow event delineation method

The rainfall timeseries must have a temporal resolution of 5 or 10 min and be previously separated into events (see Section 2.3.2 Rainfall Event Delineation), as the start and end of the events serve as input. The trenchflow record must have, or be resampled to, a time resolution of 10 min. The method was written using MATLAB (R2021b) (The MathWorks Inc, 2021) and the commented sourcecode is available upon request (Section 8).

The flowchart in Fig. B1, outlines the steps taken to detect the start and end points of the events, whereas Fig. B2 and Fig. B3 further illustrate the moving windows and criteria used in the process. The start is detected as follows:

[1] The time series is scanned from the start to the end + 6 h of *every* rainfall event to evaluate if an "unusual" increase in discharge (Q), which indicates the start of an SSF event, occurs. Six hours are chosen due to the defined MIT of 6 h.

[2] During the scan, it is tested if baseflow, computed using a 5 h backward moving average $(\overline{Q_B})$ of the trenchflow (Q) (i.e. arithmetic average between Q_i and $Q_{i-300min}$), is present. This is:

$$\overline{Q_B}_{i-10min} > 0 \qquad \text{(B1)}$$

[3] If no baseflow is detected, the algorithm tests the time series for flow onset; this is:

$$Q_i > 0 \qquad \text{(B2)}$$

- If an increase is found, the position is marked as the start of a new event and the scanning stops;
- else, the scanning continues up to the end of the rainfall event + 6 h.

https://doi.org/10.5194/egusphere-2025-5110
Preprint. Discussion started: 9 December 2025

[4] If baseflow is present, the code evaluates if there is any significant (i.e. "unusual") increase in discharge by: calculating short (10 min) and long (60 min) forward moving averages ($\overline{Q_{FS}}$ and $\overline{Q_{FL}}$) (i.e. arithmetic average from Q_i to $Q_{i+10min}$ and Q_i to $Q_{i+60min}$, respectively), computing the differences between $\overline{Q_B}$ of the previous timestep and $\overline{Q_{FS}}$ as well as $\overline{Q_{FL}}$

$$\Delta Q_{S_i} = \overline{Q_{FS}}_i - \overline{Q_B}_{i-10min} \tag{B3}$$

$$\Delta Q_{L_i} = \overline{Q_{FL}}_i - \overline{Q_B}_{i-10min} \tag{B4}$$

and evaluating if ΔQ_S and ΔQ_L are both above a certain threshold Q_T

$$\begin{cases} \Delta Q_{S_i} > Q_T \\ \Delta Q_{L_i} > Q_T \end{cases} \tag{B5}$$

as well as testing if

$$Q_i - \overline{Q_B}_{i-10min} > \left(\frac{Q_T}{2}\right). \tag{B6}$$

The latter avoids that the start is defined one timestep too early (i.e. in cases where Q_i is similar to $\overline{Q_B}_{i-10min}$ but due to the high value of $Q_{i+10min}$ the criterion in Eq. B5 is fulfilled), as the start has to coincide with the "unusual" increase in Q.

- If the above criteria (Eq. B5 and B6) are not fulfilled the scanning continues;
- else, the time step is marked as the start of a new event and the scanning stops.

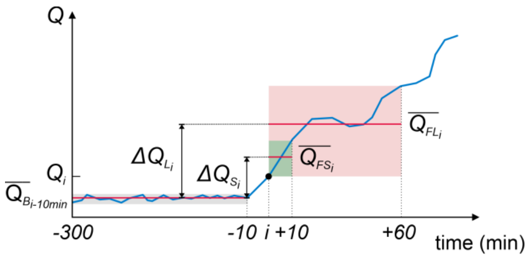

Figure B2. SSF start detection method when baseflow is present

Once the starting points of the events are defined, the ending points, which have to be followed by an "uneventful" period (i.e. a period associated with negligible changes), are detected as follows:

[5] The time series is scanned from each previously detected starting point.

[6] The change of the smoothed discharge ($\overline{Q_C}$), calculated using an 80 min centered moving average (i.e. arithmetic average between $Q_{i-40min}$ and $Q_{i+40min}$), is computed over a 4 h period ($\Delta\overline{Q_C} = \overline{Q_C}_{i+240min} - \overline{Q_C}_i$). The time series of differences $\Delta\overline{Q_C}$ is then further smoothed using a 20 min centered average approach (resulting in $\overline{\Delta Q_C}$). Next, the standard deviation of $\overline{\Delta Q_C}$ is calculated over a 4 h forward window (i.e. $\sigma\overline{\Delta Q_C}$ is equal to the sd. between $\overline{\Delta Q_C}_i$ and $\overline{\Delta Q_C}_{i+240min}$). Finally, the end of an event is marked when the following three criteria are fulfilled:

$$\begin{cases} \overline{\Delta Q_C}_{min} \le \overline{\Delta Q_C}_i \le \overline{\Delta Q_C}_{max} \\ \sigma\overline{\Delta Q_C}_i < \sigma_T \\ \overline{Q_C}_i < \left(\overline{Q_B}_{start\,-10min} + Q_T\right) \end{cases} \tag{B7}$$

where $\overline{\Delta Q_C}_{min}$ and $\overline{\Delta Q_C}_{max}$ are threshold-values that limit the acceptable change in the discharge over the next 4 h, while the threshold σ_T quantifies the acceptable variation of the discharge withing the same 4 h period. Setting low threshold values ensures that in the period following potential ending points Q does not increase nor decrease substantially. Low σ_T values in particular help to discard periods with fast-changing Q and to detect periods with well-defined trends. Due to the methodology a period of ca. 4 h from every timestep is analysed. To avoid that high “plateaus” within an event are erroneously detected as ending points the discharge value ($\overline{Q_C}$) of the ending point has to be lower than the baseflow at the start of the event ($\overline{Q_B}_{start\ -10min}$) + Q_T (threshold also used for the start detection) (i.e. it has to be less than Q_T above the baseflow). The addition of Q_T avoids that extremely shallow recession limbs hinder the detection of event ends within a reasonable time and that new slightly higher baseflows are not readily discarded for the placement of an ending point.

[7] Lastly, because the average-based method makes it difficult to pinpoint the end of an event when Q alternates between flow and no-flow conditions, the code scans backwards from the detected end point until Q is greater than zero. Once the condition is met, the endpoint is moved in front of the identified non-zero Q time step.

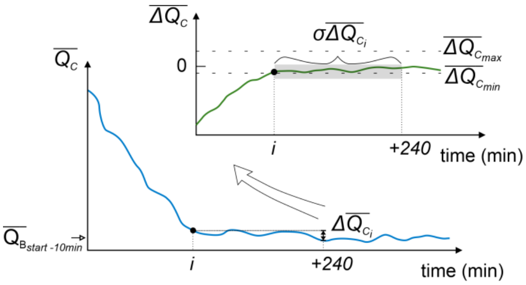

Figure B3. SSF end detection method

The above-described method was applied to the measured trenchflows using following parameters: $Q_T = 1.0$ l/h, $\sigma_T = 0.5$ l/h, $\overline{\Delta Q_C}_{max} = 0.3$ l/h and $\overline{\Delta Q_C}_{min} = -0.05$ l/h. The chosen values obviously affect the number as well as the placement of the detected starting and ending points. Therefore, they have to be carefully selected according to the observed trenchflow signal. The optimal value of Q_T and σ_T will depend, among other things, on the resolution of the flow gauge and on the amplitude of the signal noise. In this study the flow was measured using tipping bucket systems. Therefore, Q_T and σ_T were related to the flow equivalent to 1 tip/10 min which equalled to ca. 0.5 l/h.

The delineation results showed that most of the detected starts and ends of the events appear, after a visual inspection, at acceptable locations. Nevertheless, a small portion of them was placed at inappropriate locations. In fact, the method struggles to correctly locate the start when the increase in Q is very small and of similar magnitude as the signal noise, or when the start of a new event occurs during the steep recession phase of the preceding event. The latter arises due to the 5 h backward time window used to compute the “baseflow”, as higher discharge values of the falling limb would then also be included in the time window. Misplacements of ending points, on the other hand, can arise when the recession is more noisy than usual or when the new baseflow is considerably higher than the one preceding the event.

Hence, after the automatic delineation, the results had to be manually checked and were modified if necessary. This meant adding or removing a starting point as well as adjusting the position of starting and ending points. For this reason, the method is considered to be semi-automatic. To get an idea on the performance, for T1 and T3 on average ca. 4% of the starts had to be added, 15% had to be removed and 12 % of the starts had to be re-positioned, while 21% of the ends had to be re-positioned. The mentioned lengths of the periods used to calculate the averages, differences, etc., were chosen to best fit the analysed trenchflow data. Nevertheless, for different scales and other hydrological and hydrogeological settings the lengths of these periods could be adjusted.

8 Code and data availability

The data is available at https://doi.org/10.48323/vjrr0-eya46 (Thoenes, 2025).
The code will be made available upon request.

9 Author Contribution

The study was planned and designed by TB, MW, LH, BK, SA; ET contributed to the methodological development, processed, analysed and visualised the data, and wrote the first draft of the manuscript. All authors contributed to the interpretation of the data and the editing of the paper.

10 Competing interests

MW is a member of the editorial board and TB is Chief Executive Editor of the journal Hydrology and Earth System Sciences.

11 Acknowledgments

We thank all the members of the research unit “Fast and Invisible: Conquering Subsurface Stormflow through an Interdisciplinary Multi-Site Approach” (RU 5288) who helped in the construction of the trenches and instrumentation of the hillslopes as well as the technicians of Uni Freiburg (Department of Hydrology), in particular Britta Kattenstroth, for ensuring the smooth running of the operation on site. This research has been funded by the German Research Foundation (DFG) and the Austrian Science Fund (FWF) (10.55776/I5940).

12 References

Anderson, A. E., Weiler, M., Alila, Y., and Hudson, R. O.: Dye staining and excavation of a lateral preferential flow network, Hydrol. Earth Syst. Sci., 13, 935–944, https://doi.org/10.5194/hess-13-935-2009, 2009.

Angermann, L., Jackisch, C., Allroggen, N., Sprenger, M., Zehe, E., Tronicke, J., Weiler, M., and Blume, T.: Form and function in hillslope hydrology: characterization of subsurface flow based on response observations, Hydrol. Earth Syst. Sci., 21, 3727–3748, https://doi.org/10.5194/hess-21-3727-2017, 2017.

Behari, J.: Microwave Dielectric Behavior of Wet Soils, 1st ed., Springer Netherlands, Dordrecht, https://doi.org/10.1007/1-4020-3288-9, 2005.

Bishop, K. H., Grip, H., and O’Neill, A.: The origins of acid runoff in a hillslope during storm events, J. Hydrol., 116, 35–61, https://doi.org/10.1016/0022-1694(90)90114-D, 1990.

Blume, T. and van Meerveld, I.: From hillslope to stream: methods to investigate subsurface connectivity, Wiley Interdisciplinary Reviews: Water, 2, 177–198, https://doi.org/10.1002/wat2.1071, 2015.

Blume, T., Zehe, E., and Bronstert, A.: Rainfall—runoff response, event-based runoff coefficients and hydrograph separation, Hydrolog. Sci. J., 52, 843–862, https://doi.org/10.1623/hysj.52.5.843, 2007.

Blume, T., Zehe, E., and Bronstert, A.: Use of soil moisture dynamics and patterns at different spatio-temporal scales for the investigation of subsurface flow processes, Hydrol. Earth Syst. Sci., 13, 1215–1233, https://doi.org/10.5194/hess-13-1215-2009, 2009.

Blume, T., Chifflard, P., Achleitner, S., Hartmann, A., Hergarten, S., Hopp, L., Kohl, B., Leese, F., Van Meerveld, I., Reinhardt-Imjela, C., and Weiler, M.: Brief Communication: Investigating the invisible subsurface stormflow process through a thorough and systematic study across sites and scales, https://doi.org/10.5194/egusphere-2025-4424, 29 September 2025.

Brasil, J. B., Guerreiro, M. S., Andrade, E. M. de, de Queiroz Palácio, H. A., Medeiros, P. H. A., and Ribeiro Filho, J. C.: Minimum Rainfall Inter-Event Time to Separate Rainfall Events in a Low Latitude Semi-Arid Environment, Sustainability, 14, 1721, https://doi.org/10.3390/su14031721, 2022.

Buttle, J. M. and Turcotte, D. S.: Runoff Processes on a Forested Slope on the Canadian Shield, Hydrol. Res., 30, 1–20, https://doi.org/10.2166/nh.1999.0001, 1999.

Chan, C. Y. and Knight, R. J.: Determining water content and saturation from dielectric measurements in layered materials, Water Resour. Res., 35, 85–93, https://doi.org/10.1029/1998WR900039, 1999.

Detty, J. M. and McGuire, K. J.: Threshold changes in storm runoff generation at a till-mantled headwater catchment, Water Resour. Res., 46, W07525, https://doi.org/10.1029/2009WR008102, 2010.

Dickinson, W. T. and Whiteley, H.: Watershed areas contributing to runoff, IAHS publ, 96, 12–26, 1970.

Du, E., Rhett Jackson, C., Klaus, J., McDonnell, J. J., Griffiths, N. A., Williamson, M. F., Greco, J. L., and Bitew, M.: Interflow dynamics on a low relief forested hillslope: Lots of fill, little spill, J. Hydrol., 534, 648–658, https://doi.org/10.1016/j.jhydrol.2016.01.039, 2016.

Dunkerley, D.: Identifying individual rain events from pluviograph records: a review with analysis of data from an Australian dryland site, Hydrol. Process., 22, 5024–5036, https://doi.org/10.1002/hyp.7122, 2008.

Freer, J., McDonnell, J. J., Beven, K. J., Peters, N. E., Burns, D. A., Hooper, R. P., Aulenbach, B., and Kendall, C.: The role of bedrock topography on subsurface storm flow, Water Resour. Res., 38, 1269, https://doi.org/10.1029/2001WR000872, 2002.

Fu, C., Chen, J., Jiang, H., and Dong, L.: Threshold behavior in a fissured granitic catchment in southern China: 1. Analysis of field monitoring results, Water Resour. Res., 49, 2519–2535, https://doi.org/10.1002/wrcr.20191, 2013.

Guo, L., Chen, J., and Lin, H.: Subsurface lateral preferential flow network revealed by time-lapse ground-penetrating radar in a hillslope, Water Resour. Res., 50, 9127–9147, https://doi.org/10.1002/2013WR014603, 2014.

Haga, H., Matsumoto, Y., Matsutani, J., Fujita, M., Nishida, K., and Sakamoto, Y.: Flow paths, rainfall properties, and antecedent soil moisture controlling lags to peak discharge in a granitic unchanneled catchment, Water Resour. Res., 41, W12410, https://doi.org/10.1029/2005WR004236, 2005.

Han, X., Liu, J., Srivastava, P., Mitra, S., and He, R.: Effects of critical zone structure on patterns of flow connectivity induced by rainstorms in a steep forested catchment, J. Hydrol., 587, 125032, https://doi.org/10.1016/j.jhydrol.2020.125032, 2020.

Heller, K. and Kleber, A.: Hillslope runoff generation influenced by layered subsurface in a headwater catchment in Ore Mountains, Germany, Environ. Earth Sci., 75, 943, https://doi.org/10.1007/s12665-016-5750-y, 2016.

Hopp, L. and McDonnell, J. J.: Connectivity at the hillslope scale: Identifying interactions between storm size, bedrock permeability, slope angle and soil depth, J. Hydrol., 376, 378–391, https://doi.org/10.1016/j.jhydrol.2009.07.047, 2009.

Hrnčíř, M., Šanda, M., Kulasová, A., and Císlerová, M.: Runoff formation in a small catchment at hillslope and catchment scales, Hydrol. Process., 24, 2248–2256, https://doi.org/10.1002/hyp.7614, 2010.

Hübner, R., Günther, T., Heller, K., Noell, U., and Kleber, A.: Impacts of a capillary barrier on infiltration and subsurface stormflow in layered slope deposits monitored with 3-D ERT and hydrometric measurements, Hydrol. Earth Syst. Sci., 21, 5181–5199, https://doi.org/10.5194/hess-21-5181-2017, 2017.

Kienzler, P. M. and Naef, F.: Subsurface storm flow formation at different hillslopes and implications for the ‘old water paradox,’ Hydrol. Process., 22, 104–116, https://doi.org/10.1002/hyp.6687, 2008.

Kirchner, J. W.: Getting the right answers for the right reasons: Linking measurements, analyses, and models to advance the science of hydrology, Water Resour. Res., 42, W03S04, https://doi.org/10.1029/2005WR004362, 2006.

Kirsch, R. (Ed.): Groundwater Geophysics: A Tool for Hydrogeology, 2nd ed., Springer Berlin Heidelberg, Berlin, Heidelberg, https://doi.org/10.1007/978-3-540-88405-7, 2009.

Knapp, J. L. A., Berghuijs, W. R., Floriancic, M. G., and Kirchner, J. W.: Catchment hydrological response and transport are affected differently by precipitation intensity and antecedent wetness, Hydrol. Earth Syst. Sci., 29, 3673–3685, https://doi.org/10.5194/hess-29-3673-2025, 2025.

Koskelo, A. I., Fisher, T. R., Utz, R. M., and Jordan, T. E.: A new precipitation-based method of baseflow separation and event identification for small watersheds (<50km^2), J. Hydrol., 450–451, 267–278, https://doi.org/10.1016/j.jhydrol.2012.04.055, 2012.

Maidment, D. R. (Ed.): Handbook of hydrology, 6. [print.]., McGraw-Hill, New York, 1995.

McGlynn, B. L., McDonnel, J. J., and Brammer, D. D.: A review of the evolving perceptual model of hillslope flowpaths at the Maimai catchments, New Zealand, J. Hydrol., 257, 1–26, https://doi.org/10.1016/S0022-1694(01)00559-5, 2002.

McGuire, K. J., Klaus, J., and Jackson, C. R.: JAMES BUTTLE REVIEW: Interflow, subsurface stormflow and throughflow: A synthesis of field work and modelling, Hydrol. Process., 38, e15263, https://doi.org/10.1002/hyp.15263, 2024.

Meerveld, I. T. and Weiler, M.: Hillslope dynamics modeled with increasing complexity, J. Hydrol., 361, 24–40, https://doi.org/10.1016/j.jhydrol.2008.07.019, 2008.

Mei, Y. and Anagnostou, E. N.: A hydrograph separation method based on information from rainfall and runoff records, J. Hydrol., 523, 636–649, https://doi.org/10.1016/j.jhydrol.2015.01.083, 2015.

Millar, D., Buda, A., Duncan, J., and Kennedy, C.: An open-source automated workflow to delineate storm events and evaluate concentration-discharge relationships, Hydrol. Process., 36, e14456, https://doi.org/10.1002/hyp.14456, 2022.

Mosley, M. P.: Streamflow generation in a forested watershed, New Zealand, Water Resour. Res., 15, 795–806, https://doi.org/10.1029/WR015i004p00795, 1979.

Netto, A. M., Pieritz, R. A., and Gaudet, J. P.: Field study on the local variability of soil water content and solute concentration, J. Hydrol., 215, 23–37, https://doi.org/10.1016/S0022-1694(98)00259-5, 1999.

Noguchi, S., Tsuboyama, Y., Sidle, R. C., and Hosoda, I.: Subsurface runoff characteristics from a forest hillslope soil profile including macropores, Hitachi Ohta, Japan, Hydrol. Process., 15, 2131–2149, https://doi.org/10.1002/hyp.278, 2001.

Pangle, L. A., Gregg, J. W., and McDonnell, J. J.: Rainfall seasonality and an ecohydrological feedback offset the potential impact of climate warming on evapotranspiration and groundwater recharge, Water Resour. Res., 50, 1308–1321, https://doi.org/10.1002/2012WR013253, 2014.

Peel, M. C., Finlayson, B. L., and McMahon, T. A.: Updated world map of the Köppen-Geiger climate classification, Hydrol. Earth Syst. Sci., 11, 1633–1644, https://doi.org/10.5194/hess-11-1633-2007, 2007.

Penna, D., Tromp-van Meerveld, H. J., Gobbi, A., Borga, M., and Dalla Fontana, G.: The influence of soil moisture on threshold runoff generation processes in an alpine headwater catchment, Hydrol. Earth Syst. Sci., 15, 689–702, https://doi.org/10.5194/hess-15-689-2011, 2011.

Penna, D., Van Meerveld, H. J., Oliviero, O., Zuecco, G., Assendelft, R. S., Dalla Fontana, G., and Borga, M.: Seasonal changes in runoff generation in a small forested mountain catchment, Hydrol. Process., 29, 2027–2042, https://doi.org/10.1002/hyp.10347, 2015.

Peters, D. L., Buttle, J. M., Taylor, C. H., and LaZerte, B. D.: Runoff Production in a Forested, Shallow Soil, Canadian Shield Basin, Water Resour. Res., 31, 1291–1304, https://doi.org/10.1029/94WR03286, 1995.

Peters, N. E. and Ratcliffe, E. B.: Tracing Hydrologic Pathways Using Chloride at the Panola Mountain Research Watershed, Georgia, USA, Water, Air, and Soil Pollution, 105, 263–275, https://doi.org/10.1023/A:1005082332332, 1998.

Pyschik, J. and Weiler, M.: Detecting the occurrence of preferential flow in soils with stable water isotopes, https://doi.org/10.5194/egusphere-2025-2411, 4 June 2025.

LGRB-Kartenviewer: https://maps.lgrb-bw.de/, last access: 26 August 2024.

Roth, K., Schulin, R., Flühler, H., and Attinger, W.: Calibration of time domain reflectometry for water content measurement using a composite dielectric approach, Water Resour. Res., 26, 2267–2273, https://doi.org/10.1029/WR026i010p02267, 1990.

Šanda, M. and Císlerová, M.: Transforming Hydrographs in the Hillslope Subsurface, J. Hydrol. Hydromech., 57, 264–275, https://doi.org/10.2478/v10098-009-0023-z, 2009.

Schmidt, S. A. and Ahn, C.: A Comparative Review of Methods of Using Soil Colors and their Patterns for Wetland Ecology and Management, Commun. Soil Sci. Plan., 50, 1293–1309, https://doi.org/10.1080/00103624.2019.1604737, 2019.

Sidle, R. C., Tsuboyama, Y., Noguchi, S., Hosoda, I., Fujieda, M., and Shimizu, T.: Seasonal hydrologic response at various spatial scales in a small forested catchment, Hitachi Ohta, Japan, J. Hydrol., 168, 227–250, https://doi.org/10.1016/0022-1694(94)02639-S, 1995.

Smirnova, M. A. and Kozlov, D. N.: Soil Properties as Indicators of Soil Water Regime: A Review, Eurasian Soil Sc., 56, 306–320, https://doi.org/10.1134/S1064229322602396, 2023.

Stewart, R. D., Liu, Z., Rupp, D. E., Higgins, C. W., and Selker, J. S.: A new instrument to measure plot-scale runoff, Geosci. Instrum. Method. Data Syst., 4, 57–64, https://doi.org/10.5194/gi-4-57-2015, 2015.

Tabari, H.: Climate change impact on flood and extreme precipitation increases with water availability, Sci. Rep., 10, 13768, https://doi.org/10.1038/s41598-020-70816-2, 2020.

Tani, M.: Runoff generation processes estimated from hydrological observations on a steep forested hillslope with a thin soil layer, J. Hydrol., 200, 84–109, https://doi.org/10.1016/S0022-1694(97)00018-8, 1997.

The MathWorks Inc: MATLAB version: 9.11.0 (R2021b), 2021.

Thoenes, E.: Rainfall and subsurface stormflow event characteristics (1.0.0), https://doi.org/10.48323/VJRR0-EYA46, 2025.

Topp, G. C., Davis, J. L., and Annan, A. P.: Electromagnetic determination of soil water content: Measurements in coaxial transmission lines, Water Resour. Res., 16, 574–582, https://doi.org/10.1029/WR016i003p00574, 1980.

Tromp-van Meerveld, H. J. and McDonnell, J. J.: Threshold relations in subsurface stormflow: 1. A 147-storm analysis of the Panola hillslope, Water Resour. Res., 42, W02410, https://doi.org/10.1029/2004WR003778, 2006a.

Tromp-van Meerveld, H. J. and McDonnell, J. J.: Threshold relations in subsurface stormflow: 2. The fill and spill hypothesis, Water Resour. Res., 420, W02411, https://doi.org/10.1029/2004WR003800, 2006b.

Tsuboyama, Y., Sidle, R. C., Noguchi, S., and Hosoda, I.: Flow and solute transport through the soil matrix and macropores of a hillslope segment, Water Resour. Res., 30, 879–890, https://doi.org/10.1029/93WR03245, 1994.

Uchida, T., Tromp-van Meerveld, I., and McDonnell, J. J.: The role of lateral pipe flow in hillslope runoff response: an intercomparison of non-linear hillslope response, J. Hydrol., 311, 117–133, https://doi.org/10.1016/j.jhydrol.2005.01.012, 2005.

Uhlemann, S., Peruzzo, L., Chou, C., Williams, K. H., Wielandt, S., Wang, C., Falco, N., Wu, Y., Carr, B., Meldrum, P., Chambers, J., and Dafflon, B.: Variations in Bedrock and Vegetation Cover Modulate Subsurface Water Flow Dynamics of a Mountainous Hillslope, Water Resour. Res., 60, e2023WR036137, https://doi.org/10.1029/2023WR036137, 2024.

Weast, R.C: Handbook of Physics and Chemistry, 67th ed., CRC Press, Boca Raton, FL, USA, 1986.

Wei, L., Qiu, Z., Zhou, G., Kinouchi, T., and Liu, Y.: Stormflow threshold behaviour in a subtropical mountainous headwater catchment during forest recovery period, Hydrol. Process., 34, 1728–1740, https://doi.org/10.1002/hyp.13658, 2020.

Weiler, M. and McDonnell, J.: Virtual experiments: a new approach for improving process conceptualization in hillslope hydrology, J. Hydrol., 285, 3–18, https://doi.org/10.1016/S0022-1694(03)00271-3, 2004.

Weiler, M. and McDonnell, J.: Conceptualizing lateral preferential flow networks and simulating the effects on gauged and ungauged hillslopes, Water Resour. Res., 430, W03403, https://doi.org/10.1029/2006WR004867, 2007.

Weiler, M. and Naef, F.: Simulating surface and subsurface initiation of macropore flow, J. Hydrol., 273, 139–154, https://doi.org/10.1016/S0022-1694(02)00361-X, 2003.

Weiler, M., McDonnell, J., van Meerveld, I., and Uchida, T.: Subsurface Stormflow, in: Encyclopedia of Hydrological Sciences, vol. 3, https://doi.org/10.1002/0470848944.hsa119, 2006.

Wienhöfer, J. and Zehe, E.: Predicting subsurface stormflow response of a forested hillslope – the role of connected flow paths, Hydrol. Earth Syst. Sci., 18, 121–138, https://doi.org/10.5194/hess-18-121-2014, 2014.

Wraith, J. M. and Or, D.: Temperature effects on soil bulk dielectric permittivity measured by time domain reflectometry: Experimental evidence and hypothesis development, Water Resour. Res., 35, 361–369, https://doi.org/10.1029/1998WR900006, 1999.

Zadhoush, H., Giannopoulos, A., and Giannakis, I.: Optimising the Complex Refractive Index Model for Estimating the Permittivity of Heterogeneous Concrete Models, Remote Sensing, 13, 723, https://doi.org/10.3390/rs13040723, 2021.

Zhang, G., Cui, P., Gualtieri, C., Zhang, J., Ahmed Bazai, N., Zhang, Z., Wang, J., Tang, J., Chen, R., and Lei, M.: Stormflow generation in a humid forest watershed controlled by antecedent wetness and rainfall amounts, J. Hydrol., 603, 127107, https://doi.org/10.1016/j.jhydrol.2021.127107, 2021.

1030 Zwartendijk, B. W., Van Meerveld, H. J., Teuling, A. J., Ghimire, C. P., and Bruijnzeel, L. A.: Rainfall-runoff responses and hillslope moisture thresholds for an upland tropical catchment in Eastern Madagascar subject to long-term slash-and-burn practices, Hydrol. Process., 37, e14937, https://doi.org/10.1002/hyp.14937, 2023.